



## Capillary-driven binding of thin triangular prisms at fluid interfaces

Journal:	<i>Soft Matter</i>
Manuscript ID	SM-ART-02-2018-000271.R1
Article Type:	Paper
Date Submitted by the Author:	28-Mar-2018
Complete List of Authors:	Ferrar, Joseph; University of Michigan, Chemical Engineering Bedi, Desphreet; University of Michigan, Physics; Brandeis University, Martin Fisher School of Physics Zhou, Shangnan; University of Michigan, Physics; Stanford University, Theoretical Physics and Department of Physics Zhu, Peijun; University of Michigan, Physics; University of Pittsburgh, Physics and Astronomy Mao, Xiaoming; University of Michigan, Physics Solomon, Michael; University of Michigan, Chemical Engineering

1  
2  
3  
4  
5  
6  
7  
8  
9  
10  
11  
12  
13  
14  
15  
16  
17  
18

## Capillary-driven binding of thin triangular prisms at fluid interfaces

Joseph A. Ferrar<sup>1</sup>, Deshpreet S. Bedi<sup>2,3</sup>, Shangnan Zhou<sup>2,4</sup>, Peijun Zhu<sup>2,5</sup>, Xiaoming Mao<sup>2\*</sup>, and Michael J. Solomon<sup>1\*</sup>

<sup>1</sup> Department of Chemical Engineering, University of Michigan, Ann Arbor, MI 48109

<sup>2</sup> Department of Physics, University of Michigan, Ann Arbor, MI 48109

<sup>3</sup> Martin Fisher School of Physics, Brandeis University, Waltham, MA 02454

<sup>4</sup> Theoretical Physics and Department of Physics, Stanford University, Stanford, CA 94305

<sup>5</sup> Department of Physics and Astronomy, University of Pittsburgh, Pittsburgh, Pennsylvania 15260

(\*Corresponding Author: [maox@umich.edu](mailto:maox@umich.edu) and [mjsolo@umich.edu](mailto:mjsolo@umich.edu))

## 1 **Abstract**

2 We observe capillary-driven binding between thin, equilateral triangular prisms at  
3 a flat air-water interface. The edge length of the equilateral triangle face is  $120\ \mu\text{m}$ , and  
4 the thickness of the prism is varied between 2 and  $20\ \mu\text{m}$ . For thickness to length (T/L)  
5 ratios of  $1/10$  or less, pairs of triangles preferentially bind in either a tip-to-tip or tip-to-  
6 midpoint edge configurations; for pairs of prisms of thickness  $T/L = 1/5$ , the tip of one  
7 triangle binds to any position along the other triangle's edge. The distinct binding  
8 configurations for small T/L ratios result from physical bowing of the prisms, a property  
9 that arises during their fabrication. When bowed prisms are placed at the air-water  
10 interface, two distinct polarity states arise: prisms either sit with their center of mass  
11 above or below the interface. The interface pins to the edge of the prism's concave face,  
12 resulting in an interface profile that is similar to that of a capillary hexapole, but with  
13 important deviations close to the prism that enable directed binding. We present  
14 corresponding theoretical and numerical analysis of the capillary interactions between  
15 these prisms and show how prism bowing and contact-line pinning yield a capillary  
16 hexapole-like interaction that results in the two sets of distinct, highly-directional binding  
17 events. Prisms of all T/L ratios self-assemble into space-spanning open networks; the  
18 results suggest design parameters for the fabrication of building blocks of ordered open  
19 structures such as the Kagome lattice.

20

21

## 1 Introduction

2 Attractive, long-range capillary interactions arise between particles at an air-liquid  
3 or liquid-liquid interface because they minimize the free energy generated by the particle-  
4 induced curvature of the interface.<sup>1-7</sup> Self-assembly of colloidal, granular, and  
5 millimeter-scale particles has been observed at both air-water and oil-water interfaces due  
6 to such capillary-induced pair attractions. At the colloidal scale, short-range electrostatic  
7 repulsions also influence self-assembly.<sup>8-10</sup> Recently, spatially anisotropic capillary  
8 attractions have been used to produce ordered particle chains and complex open networks  
9 at fluid interfaces. For example, colloidal ellipsoids at oil-water and air-water interfaces  
10 form such structures. Particle configurations that arise at the interface are dependent on  
11 particle surface geometry, chemistry, and wettability.<sup>10,11</sup> For example, cylinders and  
12 related anisotropic shapes assemble into chains at an oil-water interface, with the specific  
13 particle faces that bind determined by the curvature of the particle face. In these cases,  
14 the spatial anisotropy of the capillary interaction is a consequence of differences in the  
15 local curvature of the particle.<sup>12,13</sup> Specifically, cylindrical particles at an oil-water  
16 interface generate an elliptical quadrupolar interaction in the far field: the interface  
17 deforms in one direction at the flat ends of the cylinder and the opposite direction at the  
18 curved edges. These deformations yield attractive capillary interactions between faces  
19 with like-curvature and repulsions between faces with opposite-curvature.<sup>12,13</sup>

20 Capillary-driven self-assembly therefore is a path to the bottom-up assembly of  
21 open and network structures. Such structures are targets for self-assembly due to  
22 interesting and potentially useful properties, ranging from photonic bandgaps to unusual  
23 mechanical response, that arise from the incorporation of voids into material structures.<sup>14-</sup>  
24 <sup>17</sup> These networks and voids deform in ways that significantly differ from close-packed  
25 structures, and can lead to mechanical properties such as negative Poisson's ratio and  
26 rigidity at ultra-low density. For example, open networks of colloidal ellipsoids  
27 assembled at a fluid-fluid interface exhibited a significantly enhanced low frequency  
28 modulus as compared to close-packed networks of colloidal spheres at similar particle  
29 concentrations.<sup>10</sup>

30 Current methods to fabricate open networks include the above described  
31 capillary-driven assembly of colloidal ellipsoids,<sup>10,11</sup> and polymer-molded  
32 microhexagram prisms,<sup>18</sup> millimeter-scale branched shapes produced by 3D printing,<sup>19</sup>  
33 self-assembly of patchy colloidal spheres,<sup>20-22</sup> and top-down approaches on the granular  
34 and millimeter-scale such as polymeric 3D-printing,<sup>23</sup> quasi-2D-polymer molding<sup>24</sup> and  
35 lithography.<sup>25</sup> Bottom-up self-assembly methods can be advantageous compared to these  
36 top-down methods, because of the potential scalability of self-assembly processes.<sup>26,27</sup>

37 Here we investigate the possibility of using a hexapolar-like interaction generated  
38 between pairs of thin, triangular microprisms to self-assemble space-spanning open  
39 networks at low particle concentrations. Assembly of such a rigid, stabilizing network by  
40 control of lateral interactions could yield complex fluids with useful bulk and interfacial  
41 rheological properties of interest in a variety of fields and industries, such as food  
42 science, drug delivery, and petrochemical processing.<sup>28-31</sup>

1 Thin prisms – quasi-2D shapes with finite but small thickness – can generate  
 2 capillary interactions at fluid-fluid interfaces if sufficient interface deformation is induced  
 3 at the prism edges. The symmetry of thin, triangular prisms indicates that the interaction  
 4 will be similar to that of capillary hexapoles when these prisms are not too close. This  
 5 interaction may lead to binding of the triangles at vertices and yield ordered structures  
 6 such as the kagome and the twisted kagome lattices – a family of isostatic structures with  
 7 a unit cell of two inverted triangles (Figure 1). These kagome lattices are known to  
 8 display unusual mechanical properties such as a negative Poisson's ratio and floppy edge  
 9 modes.<sup>15,17,20,32–36</sup> To improve the prospects for assembling such complex open structures  
 10 – either ordered or disordered – the pair-binding behavior of thin homogenous  
 11 micropillars at interfaces should be investigated. Better understanding of the transient  
 12 and steady-state binding can identify conditions for which ordered and/or disordered  
 13 networks (Figure 1) might occur; each structural family might itself exhibit interesting  
 14 mechanical properties.<sup>10</sup> Open, planar networks – both disordered and ordered – are  
 15 therefore interesting targets for interfacial self-assembly.

16 Here we observe capillary-driven binding of thin, triangular prisms, with edge

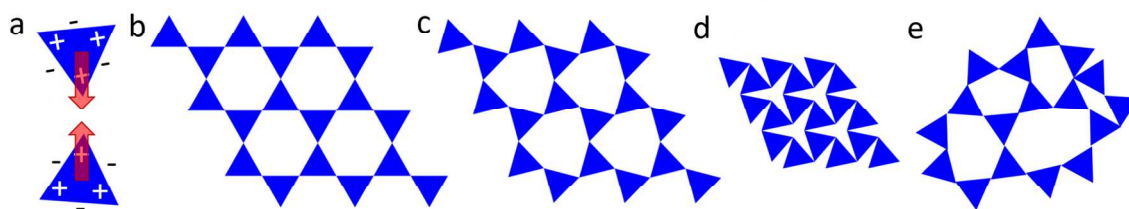


*Figure 1 Hexapole-like capillary interaction between triangles may lead to the self-assembly of kagome lattices. (a) Hexapole-like interactions between triangles (positive at tips and negative at edges) cause tip-to-tip binding. (b) The kagome lattice where edges of triangles form straight lines. (c,d) two twisted kagome lattices with different twisting angle. These different versions of the kagome lattices are related by a soft deformation which only changes the bond angle, which leads to the negative Poisson's ratio of this structure. (e) Depending on the strength of the hexapole-like interaction, disordered assemblies of triangles may also appear.*

17 lengths  $\sim 120 \mu\text{m}$  and thicknesses between  $2.5$  and  $20 \mu\text{m}$  at an air-water interface. The  
 18 pairwise interaction between prisms is measured and modeled. The prisms are produced  
 19 by polymeric photolithography; the anisotropic, directional interactions are introduced by  
 20 the unexpected generation of a capillary hexapole, which arises due to the 2D triangular  
 21 shape and the contact line curvature induced by edgewise bowing of the prisms that is  
 22 introduced at the time of synthesis. We record the different types of binding events  
 23 observed between the vertices and flat edges of the interacting prisms. The type of  
 24 binding event is predictable from the up/down polarity of prism attachment to the  
 25 interface, which is well characterized by imaging out-of-plane and by environmental  
 26 scanning electron microscopy. From the prism shape and bowed radius of curvature, we  
 27 compute the interface geometry and the resulting capillary interaction numerically. We  
 28 find that the capillary interaction is similar to hexapolar interaction in the far field, but  
 29 deviates from ideal hexapoles in the near field such that the variability of the potential is  
 30 largest at the tips. We also simulate trajectories of prism binding events numerically  
 31 using the potential we calculated, and we obtain good agreement with qualitative features

1 of the experimental results. These results can inform the structural design of complex  
2 open networks from interfacial building blocks.

### 3 **Materials & Methods**

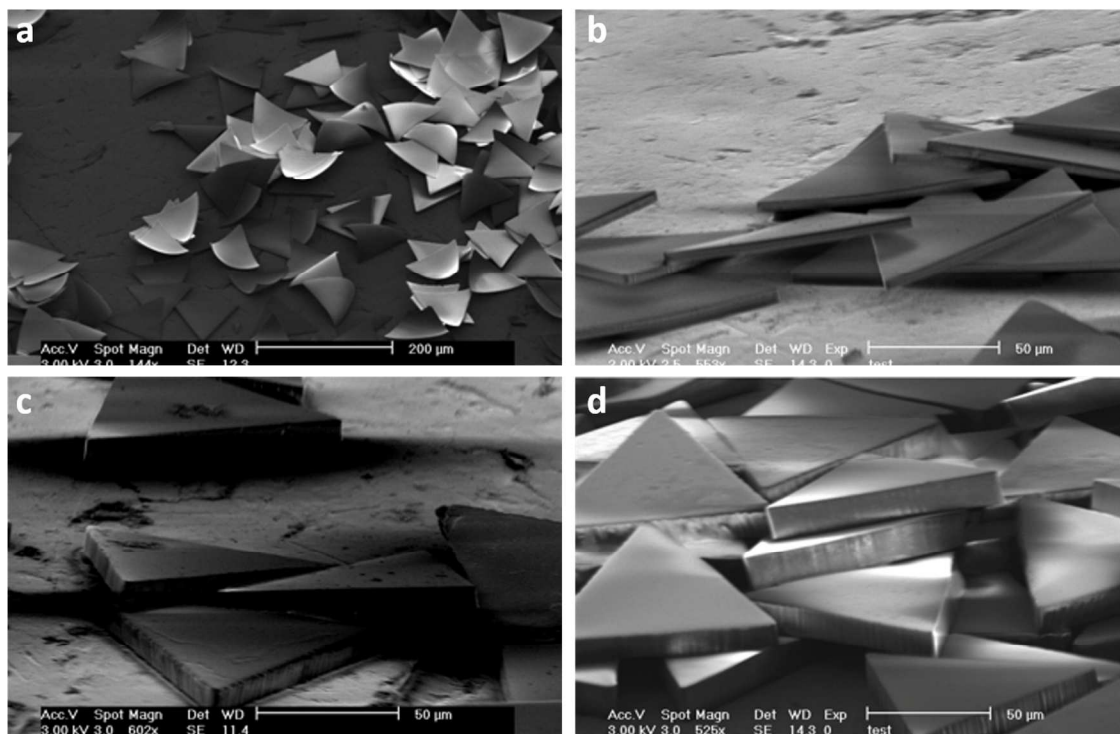
#### 4 *Prism Fabrication*

5 Prisms are fabricated via SU-8 photolithography.<sup>12,13,37</sup> First, a sacrificial release  
6 layer of Omnicoat (Microchem Corp.) is spun onto a glass wafer (D-263 borosilicate  
7 glass, Precision Glass & Optics) and baked at 200 C until cured to a thickness of tens of  
8 nanometers (1-2 minutes). After cooling to room temperature, SU-8 2000 series  
9 photoresist (Microchem Corp.) is spun on top of the Omnicoat layer to the desired prism  
10 thickness and baked at 95 C until cured (~2-5 minutes depending on resist thickness).  
11 Next, the wafer is exposed to UV light (365 and 405 nm) through a chrome photomask  
12 that encodes the prism pattern (Fineline Imaging) until exposure energies of 60-150 mJ  
13 (depending on resist thickness) are achieved. The wafer is then heated at 95 C for 2-5  
14 minutes (depending on resist thickness) to ensure adequate cross-linking of the exposed  
15 photoresist.

16 The wafer is immersed in SU-8 developer solution (Microchem Corp.) until the  
17 non-photopolymerized SU-8 is washed away (~1-5 minutes depending on resist  
18 thickness), leaving the cross-linked prisms immobilized on top of the release layer. The  
19 wafer is exposed to oxygen plasma for 20 minutes, which facilitates release of the prisms  
20 into isopropanol. The prisms are stored in isopropanol, where they remain stable for  
21 several weeks. This process yields approximately  $10^6$  prisms per fabrication. Figure  
22 shows the 4 types of equilateral triangular prisms fabricated. All prisms have an edge  
23 length of 120  $\mu\text{m}$ , and thickness of: (a) 2.5  $\mu\text{m}$ , (b) 5  $\mu\text{m}$ , (c) 12  $\mu\text{m}$ , and (d) 20  $\mu\text{m}$ . The  
24 ratio of the thickness (T) to length (L) of the prisms is a characteristic parameter; we  
25 hereafter refer to each type of prism as: (a)  $T/L = 1/50$ , (b)  $T/L = 1/25$ , (c)  $T/L = 1/10$ ,  
26 and (d)  $T/L = 1/5$ .

#### 27 *Placement of prisms at the air-water interface*

28 A flat interface is formed between air and deionized water in a chamber (Thermo  
29 Scientific Lab-Tek II, 2 Chamber, coverslip 0.13-0.17  $\mu\text{m}$  thick, type 1.5) of dimension  
30 2.0 x 2.0 cm, mounted on to the stage of a Nikon A1Rsi confocal microscope. The  
31 chamber's large experimental area and acrylic walls allow for a flat air-water interface to  
32 form – without the need for surface modification of the chamber – through careful  
33 placement of water in the chamber with a transfer pipette. The walls of the chamber are  
34 manually wet prior to filling the center of the chamber with water, in order to prevent  
35 uneven attachment of the interface to the walls of the chamber. 10  $\mu\text{L}$  of the prism stock  
36 solution is carefully placed in one or two drops at the air-water interface using a gas-tight  
37 Hamilton 100  $\mu\text{L}$  syringe.



1

2 *Figure 2 SEM images of thin, equilateral triangular microprisms from SU-8 epoxy resin.*  
 3 *Equilateral triangle (edge length,  $L = 120 \mu\text{m}$ ) prisms of varying thickness ( $T$ ) a)  $T \sim 2.5$   
 4  $\mu\text{m}$ ,  $T/L = 1/50$ , b)  $T \sim 5 \mu\text{m}$ ,  $T/L = 1/25$ , c)  $T \sim 12 \mu\text{m}$ ,  $T/L = 1/10$ , d)  $T \sim 20 \mu\text{m}$ ,  $T/L =$   
 5  $1/5$ .*

6 *Observation of binding events with optical and reflection microscopy*

7 The interface is imaged with the transmission and 488 nm reflection channels of a  
 8 Nikon A1Rsi confocal microscope (10x objective,  $NA = 0.25$ ) in a square region of 1270  
 9 x 1270  $\mu\text{m}$ . Images of pair binding and assembly are acquired at frame rates of 15  
 10 frames per second (fps) for prisms of  $T/L \geq 1/25$  and 30 fps for  $T/L = 1/50$ . For pair  
 11 binding experiments, prism positions, relative orientations, and trajectories are tracked by  
 12 least square fitting of prism edges, as detected by scikit-image (<http://scikit-image.org/>).

13 *Quantifying capillary attraction energies through observation of interface deformation*  
 14 *with environmental SEM*

15 Environmental SEM (eSEM, FEI Quanta 3D) is used to observe interface  
 16 deformation and curvature around the edges of the prisms. A gel trapping technique is  
 17 used to immobilize prisms at the interface.<sup>13,38</sup> Briefly, gellan gum, which was generously  
 18 supplied as a gift from CP Kelco, (low acyl Kelcogel, 2 wt. %) is dissolved in deionized  
 19 water at 95 °C. The gellan solution remains fluid at temperatures greater than 50 °C.  
 20 The gellan solution is placed into an eSEM imaging chamber at 70 °C, and prisms are  
 21 spread at the interface. The imaging chamber is at room temperature, a condition at  
 22 which the gellan solution crosslinks, immobilizing the prisms for later imaging. Identical  
 23 prism-prism capillary-driven binding is observed at the gellan solution-air interface as is  
 24 observed at the pure water-air interface, suggesting that the gellan solution has a

1 negligible effect on the capillary-binding mechanism, consistent with reports of right  
2 cylinders at gellan interfaces.<sup>13</sup>

### 3 *Modeling of the pairwise interaction potential using Surface Evolver*

4 In this paper, we consider the capillary interaction potential between triangular prisms,  
5 for which an analytic solution to Laplace's equation – especially close to the prisms,  
6 where simplifying assumptions cannot be made – is not available (more discussion of  
7 capillary interactions can be found in the Supplementary Information). Therefore, we use  
8 Surface Evolver, a program widely utilized to model the shape of liquid surfaces and  
9 interfaces, to numerically calculate the shape of the interface.<sup>39</sup> The solution is achieved  
10 by an algorithmic succession of steps involving gradient and conjugate gradient descent  
11 iterations and interface mesh refinements to minimize the interfacial energy subject to  
12 specific boundary conditions.

13 As we discuss in the Results section, we compute the interface shape given a pinned  
14 contact line around a bowed equilateral triangle of side length 120  $\mu\text{m}$ . In particular, this  
15 triangle is formed by the intersection of three planes containing great circles with a thin  
16 spherical shell. Specifying the behavior of the contact lines yields one set of boundary  
17 conditions; the far-field boundary condition is that the interface is flat. To allow for the  
18 condition of mechanical equilibrium to be satisfied, we do not explicitly fix the height of  
19 the far-field boundary, which, in effect, allows for changes in the relative height between  
20 the prisms and the equilibrium, unperturbed height of the interface.

21 In order to generate a potential energy landscape of a pair of interacting triangles, we run  
22 Surface Evolver simulations on a regularly-spaced grid in  $(r, \theta_1, \theta_2)$  configuration space,  
23 where  $r$  is the distance between the centers of the two triangles,  $\theta_1, \theta_2$  are the orientations  
24 of the two triangles (see Figure for their definitions). The parameter ranges are  
25  $132 \mu\text{m} \leq r \leq 360 \mu\text{m}$  and  $0^\circ \leq \theta_1, \theta_2 < 360^\circ$ , with grid spacings of 12  $\mu\text{m}$  in distance  
26 and  $5^\circ$  in orientation. The actual number of simulations needing to be run is substantially  
27 reduced by symmetries inherent in the system. Simulations are run for both prisms with  
28 the same bowing polarity and opposite bowing polarities; the definitions of bowing and  
29 polarity are introduced in the results.

### 30 *Computing prism trajectories leading to pair binding*

31 For a prism moving through a fluid at relatively slow speeds and at a low Reynolds  
32 number,  $\text{Re}$ , the drag force is given by

$$33 \quad \mathbf{F}_d = -\eta_r \dot{\mathbf{r}}. \quad (1)$$

34

35 Analogously, a prism rotating in a fluid at slow speeds experiences a drag torque,

$$36 \quad \tau_d = -\eta_\theta \dot{\theta}. \quad (2)$$

36 In these equations,  $\eta_r$  and  $\eta_\theta$  are the viscous damping coefficients for the center-of-mass  
37 and rotational degrees of freedom of the triangular prisms, respectively.

1 Assuming a quasistatic force balance on the prisms, we can equate the  
 2 corresponding drag and capillary forces to obtain the following system of differential  
 3 equations of motion for the pair of prisms. This is a valid assumption to make, as both the  
 4 Reynolds number  $Re = \rho va/\mu$ , which is a ratio of inertial forces to viscous forces within  
 5 a fluid, and the capillary number  $Ca = \mu v/\gamma$ , which is a ratio of viscous forces to surface  
 6 tension of an interface, where  $\rho$  is the density of the liquid,  $v$  is the velocity of the prism,  
 7 and  $\mu$  is the dynamic viscosity of the liquid, are quite small (for a set of characteristic  
 8 values  $\rho = 10^3 \text{ kg/m}^3$ ,  $a = 120 \text{ }\mu\text{m}$ ,  $\mu = 1.002 \times 10^{-3} \text{ Pa}\cdot\text{s}$ ,  $\gamma = 72 \times 10^{-3} \text{ N/m}$ ,  
 9 and  $v \sim 4 \times 10^{-4} \text{ m/s}$ , which is representative of the upper range of velocities observed  
 10 in the dilute binding events,  $Re \approx 0.048$  and  $Ca \approx 5.6 \times 10^{-6}$ , both of which are small  
 11 compared to unity), so that both inertia and viscous deformation of the interface can be  
 12 neglected, as in Refs. 8 and 10. In this case, hydrodynamic interactions can safely be  
 13 ignored, and the force balance equations are

14

$$\eta_r \partial_t r(t) = -\partial_r U(\theta_1, \theta_2, r) \quad (3.1)$$

$$\eta_\theta \partial_t \theta_1(t) = -\partial_{\theta_1} U(\theta_1, \theta_2, r) \quad (3.2)$$

$$\eta_\theta \partial_t \theta_2(t) = -\partial_{\theta_2} U(\theta_1, \theta_2, r) \quad (3.3)$$

15 Discretizing the time derivative of our desired quantities allows us to iteratively solve for  
 16 the trajectories of the prisms:

$$r(t_i) = r(t_{i-1}) - \frac{1}{\eta_r} \frac{\partial U}{\partial r} \Delta t \quad (4.1)$$

$$\theta_l(t_i) = \theta_l(t_{i-1}) - \frac{1}{\eta_{\theta_l}} \frac{\partial U}{\partial \theta_l} \Delta t \quad (4.2)$$

17

18 where  $i, i-1$  correspond to the  $i^{\text{th}}, (i-1)^{\text{th}}$  time-step, respectively, and  $l = 1, 2$   
 19 corresponds to the prism.

20 The partial derivatives are taken of an interpolated interaction potential using the  
 21 potential values determined via Surface Evolver on the regular  $(r, \theta_1, \theta_2)$  grid, as  
 22 discussed previously.

23 The viscous damping coefficients are not independent constants. They both  
 24 originate from the interaction between the prism and the surrounding fluid. The center of  
 25 mass drag  $\eta_r$  depends on the prism orientation and the direction of center-of-mass  
 26 motion. To our knowledge there is no literature on the fluid drag of triangular prisms, so  
 27 in this study we make a simplifying assumption that both  $\eta_r$  and  $\eta_\theta$  are constants, and we  
 28 estimate their magnitude by considering the following calculation: The work done over a  
 29 small linear translation of  $\Delta r$  due to the drag force is  $W_l = F_d \Delta r$ , while the work done  
 30 over a small rotation by  $\Delta \theta$  (in radians) due to the drag torque is given by  $W_r = \tau_d \Delta \theta$ .  
 31 We can attribute the work done by each drag to the energy required to move the fluid due  
 32 to the prism's motion. If we keep the small distance traversed by a single tip of the

1 (equilateral) triangle the same in both cases,  $\Delta r$ , then the amount of rotation associated  
 2 with that movement is given by  $\Delta\theta = \Delta r/c$ , where  $c$  is the distance from the centroid to  
 3 the tip. If the equilateral triangle has a side length of  $s$ , then  $c = s/\sqrt{3}$ . Comparing these  
 4 two cases, the amount of fluid that is moved is of the same order, which means that we  
 5 can equate  $W_l$  and  $W_r$ . We also assume that these two motions require the same amount  
 6 of time,  $\Delta t$ . In this case, we obtain

$$\eta_r \frac{\Delta r}{\Delta t} \Delta r = \eta_\theta \frac{\Delta\theta}{\Delta t} \Delta\theta, \quad (5)$$

7

8 so that the ratio between the two drag coefficients becomes

$$\frac{\eta_\theta}{\eta_r} = \left(\frac{\Delta r}{\Delta\theta}\right)^2 = c^2. \quad (6)$$

9

10 For angles measured in degrees, this equation becomes

$$\frac{\eta_{\bar{\theta}}}{\eta_r} = \left(\frac{\Delta r}{\Delta\bar{\theta}}\right)^2 = c^2 \left(\frac{\pi}{180}\right)^2. \quad (7)$$

11

12 For  $s = 120 \mu\text{m}$ ,  $c = 69.3 \mu\text{m}$  and  $\eta_{\bar{\theta}}/\eta_r = 1.46 (\mu\text{m}/^\circ)^2$ .

13 *Theoretical power-law relation for dilute binding trajectories*

14 For an experimental system exhibiting pairwise binding due to capillary  
 15 interactions, the resultant trajectory can be characterized by the form of the separation  
 16 distance  $r$  as a function of time-to-contact,  $t_c - t$ , where  $t_c$  is the first instance where the  
 17 prisms touch. If the trajectory obeys a power-law relation such that  $r \sim (t_c - t)^\beta$ , the  
 18 exponent  $\beta$  gives insight into the order of the capillary interaction, as we presently show.

19 The capillary interaction energy between two ideal multipoles is  $U_{12} \sim r^{-\alpha}$ ,  
 20 where  $\alpha = 2m$  for an interaction between two multipoles of order  $m$ . Equating the  
 21 resultant capillary force (for fixed orientations) to the viscous drag force yields a simple  
 22 first-order differential equation

$$\frac{dr}{dt} \sim r^{-(\alpha+1)}, \quad (8)$$

23

24 which can be solved to obtain the desired result that the pairwise binding trajectory  
 25 between two ideal capillary multipoles of order  $m$  is characterized by a power-law  
 26 exponent

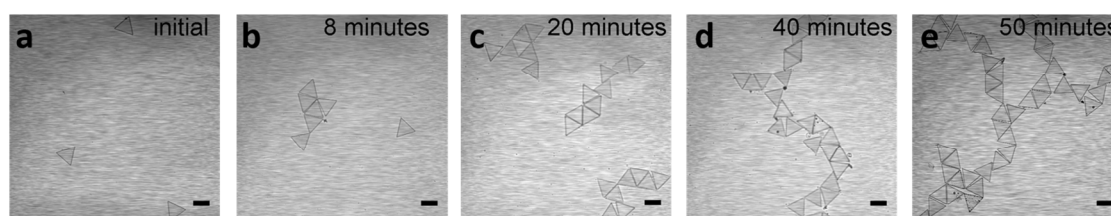
$$\beta = \frac{1}{\alpha + 2} = \frac{1}{2(m + 1)}. \quad (8)$$

1 Exponents of particular importance in this context are  $\beta = 1/6$  (two quadrupoles) and  
 2  $\beta = 1/8$  (two hexapoles).

### 3 Results

#### 4 *Capillary-driven binding of triangular prisms at a flat air-water interface*

5 Prisms of all T/L ratios undergo lateral capillary-driven binding at a flat air-water  
 6 interface. Capillary attractions yield prism-prism binding immediately upon prism  
 7 attachment at the interface. Over a period of about one hour, the prisms self-assemble  
 8 into open structures of progressively increasing size (as shown for the case of T/L = 1/25  
 9 in Figure ).

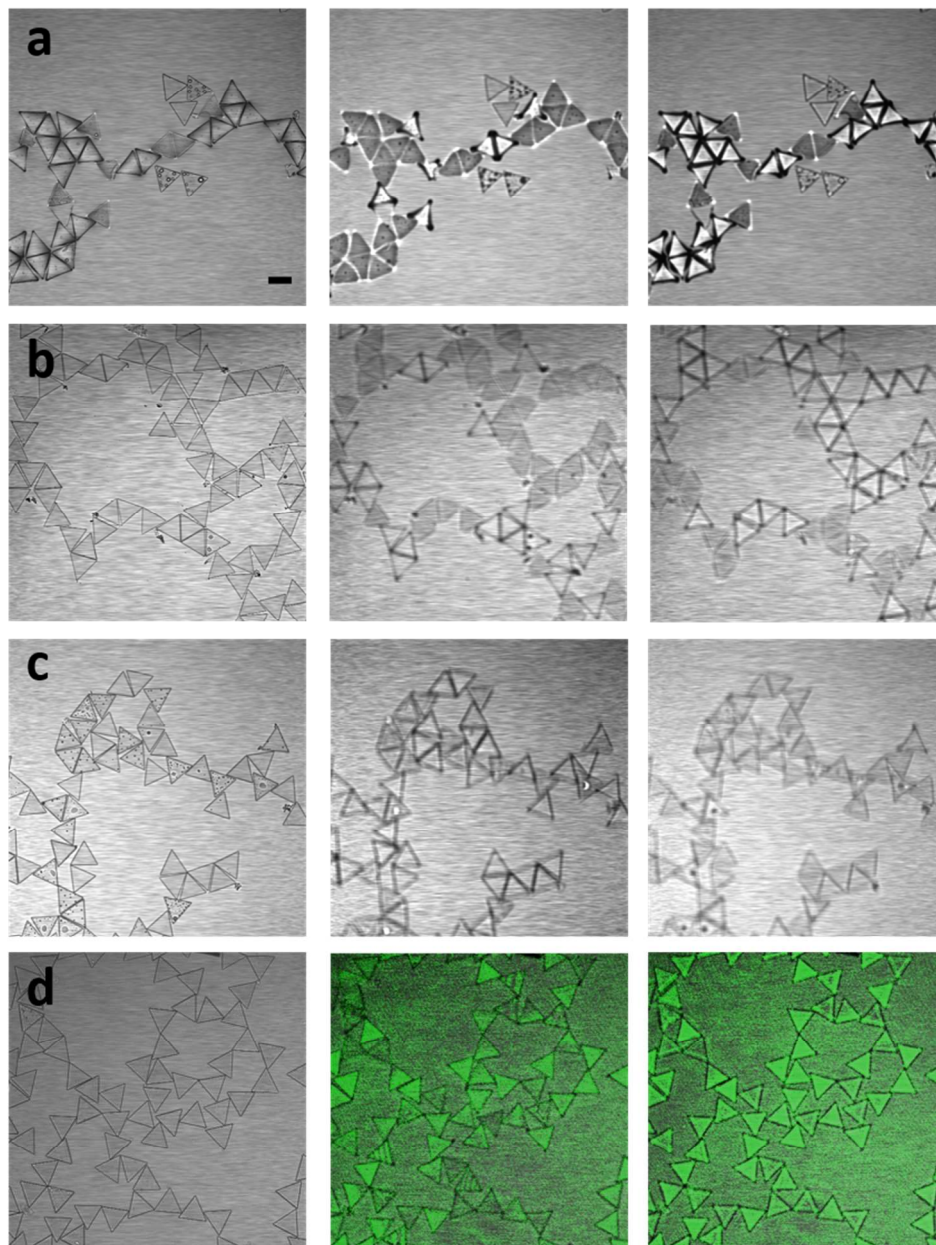


10

11 *Figure 3 Optical microscopy time-series images of capillary-driven triangular prism (T/L ~*  
 12 *1/25) binding at a flat air-water interface. a) Initial placement of prisms at interface b) 8*  
 13 *minutes after placement of prisms at interface c) 20 minutes d) 40 minutes e) 50 minutes.*  
 14 *Scale bars are 100  $\mu\text{m}$ .*

#### 15 *Polarity in interface attachment for thin prisms*

16 Figure shows 1270 x 1270  $\mu\text{m}$  regions of open, void-containing networks formed  
 17 by prisms of the four T/L ratios synthesized. Each row in Figure corresponds to a  
 18 specific T/L ratio (row 1 shows an open network formed by T/L = 1/50 prisms, row 2 is  
 19 for T/L = 1/25 prisms, row 3 is T/L = 1/10, and row 4 is T/L = 1/5). The networks span  
 20 several millimeters in space and are visible to the eye. For the three thinnest T/L ratios,  
 21 the network's steady-state microstructure (defined here as the structure which persists  
 22 after  $\geq 99\%$  of all single particles on the interface have assembled into a single,  
 23 connected network, and no further capillary-induced binding events are observed for  
 24 durations longer than a multiple of ten minutes) is comprised of a mix of dense, close-  
 25 packed regions (with numerous prisms bound edge-to-edge), long strands, and large  
 26 voids. On the other hand, relative to the thinner prisms, the network self-assembled from  
 27 T/L = 1/5 prisms contains significantly fewer prisms in close-packing configurations, less  
 28 chaining, smaller voids, and a generally more homogeneous prism density throughout the  
 29 image.



1

2 *Figure 4 Optical microscopy images of  $1270 \times 1270 \mu\text{m}^2$  regions of open, void-containing*  
3 *networks. Networks are self-assembled via capillary-driven triangular prism binding.*  
4 *Row 1 (a)  $T/L \sim 1/50$ , row 2 (b)  $T/L \sim 1/25$ , row 3 (c)  $T/L \sim 1/10$ , row 4 (d)  $T/L \sim 1/5$ .*  
5 *Column 1: single frame image of portion of network ( $1270 \times 1270 \mu\text{m}$ ), focal plane at*  
6 *air-water interface. Column 2: same single frame image of portion of network as in*  
7 *column 1, focal plane  $\sim 200 \mu\text{m}$  below air-water interface. Column 3: same single frame*  
8 *image of portion of network as in columns 1 and 2, focal plane  $\sim 200 \mu\text{m}$  above air-water*  
9 *interface. Green images in row (d) are overlays of optical and reflection microscopy; the*  
10 *reflection channel highlights differences in position of thick, apolar prisms at the flat air-*  
11 *water interface. Scale bar is  $100 \mu\text{m}$ .*

1 In the course of imaging the open networks (c.f Figure 4), the location of the  
2 microscope's focal plane relative to the air-water interface was varied and an interesting  
3 feature of the pair binding was observed. Upon varying the focal plane slightly above  
4 and below the interface, we observe that  $T/L = 1/50$ ,  $1/25$ , and  $1/10$  prisms are pinned to  
5 the interface in such a way that their centers-of-mass either sit slightly above or below the  
6 interface. The second and third columns of Fig. 4 show this kind of imaging in the same  
7  $1270 \times 1270 \mu\text{m}$  region of the open network as imaged in the first column. In column  
8 one, the microscope's focal plane is located at the air-water interface. All prisms are  
9 clear and visible, as demonstrated by their sharp, dark edges and tips, as well as their  
10 bright bodies. In the second column, the microscope's focal plane is located  $\sim 200 \mu\text{m}$   
11 below the air-water interface. For the three thinnest prisms ( $T/L = 1/50$ ,  $1/25$  and  $1/10$ ),  
12 some prisms remain clearly visible, with their dark edges and tips appearing thicker and  
13 even more discernable than in the first column and their bodies remaining bright, while  
14 all other prisms fall distinctly less visible, with their tips becoming bright and their edges  
15 and bodies appearing darker and faded.

16 In column three, the microscope's focal plane is located a similar amount *above*  
17 the air-water interface, in the opposite direction of the second column images. For the  
18 three thinnest prisms ( $T/L = 1/50$ ,  $1/25$ , and  $1/10$ ), the prisms that were clearly visible in  
19 the second column now appear faded, while the prisms that appeared faded in column  
20 two are now clearly visible. (Additionally, a very small fraction of  $T/L = 1/50$  prisms  
21 appear equally visible on both edges of the interface.)

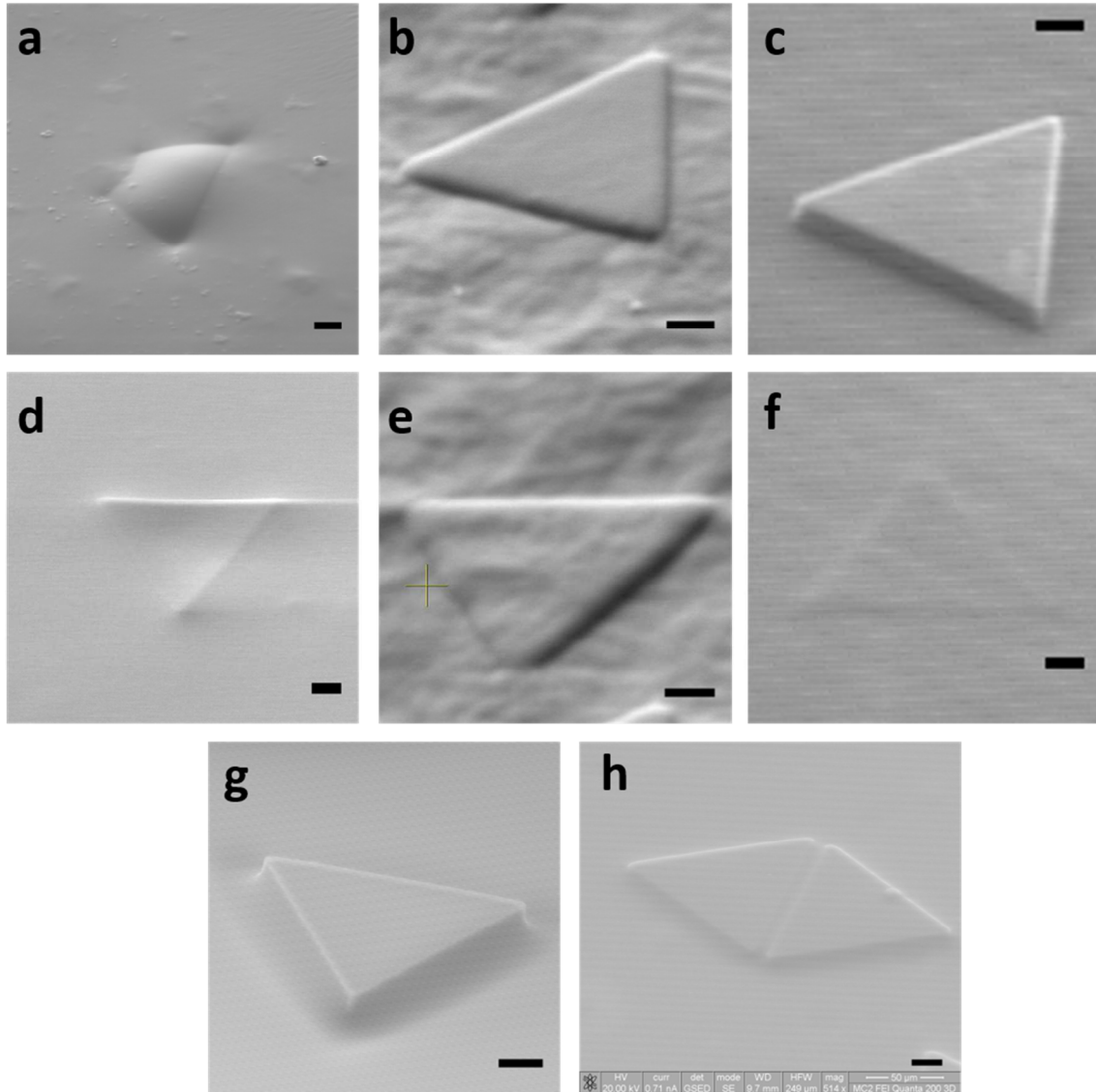
22 This visual contrast in prisms of opposite polarity is a scattering effect owing to  
23 transmission imaging, and indicates that the prisms either sit below or above the  
24 interface. In the ensuing discussion, we define this as the "polarity" of the interface  
25 attachment. A prism with positive polarity refers to a prism whose center of mass sits  
26 above the interface in the assembly experiments, while a prism with negative polarity  
27 refers to a prism whose center of mass sits below the interface.

28 Although the three thinnest prisms are divided into populations located above and  
29 below the interface, the thickest prisms ( $T/L = 1/5$ ) do not exhibit such visible vs. faded  
30 polarity; these prisms all appear equally visible relative to one another in both columns  
31 two and three. The relative image quality for the  $T/L = 1/5$  prisms appears better below  
32 the interface (column two) than above (column three), suggesting that all these prisms are  
33 situated slightly below the interface.

34 For future studies, the visual inspection criteria described above could be more  
35 efficiently implemented via image analysis. For example, a combination of the particle  
36 centroid identification algorithms of Crocker and Grier could be combined with simple  
37 edge detection algorithms to differentiate prisms that are visible vs. faded given the  
38 location of the focal plane.<sup>40</sup> Such algorithms would assist in the assignment of polarity  
39 in data sets where the quantity of prisms is much larger than the more limited cases of  
40 this initial investigation.

41 To further investigate the precise manner of prism interface attachment, we  
42 observe the prisms using eSEM (Figure 5). Figure 5 confirms polarity in interface  
43 attachment for  $T/L = 1/50$ ,  $1/25$ ,  $1/10$  but not for the thickest ( $T/L = 1/5$ ) prism,

1 consistent with the results from changing the optical microscopy focal plane. eSEM  
 2 images of  $T/L = 1/50$  prisms are shown in Figure 5a and d. Figure 5a shows a prism  
 3 whose center of mass lies above the gelled interface in the air phase, and Figure 5d shows  
 4 a prism whose center-of-mass lies below the gelled interface in the water phase. In  
 5 addition, significant prism bowing along each of the three prism edges is observed.



6  
 7 *Figure 5 Environmental SEM images of triangular prisms, fixed at an air-gellan/water*  
 8 *interface. Row 1: (a) - (c) prisms assigned positive polarity: (a)  $T/L = 1/50$ , (b)  $T/L =$*   
 9  *$1/25$ , (c)  $T/L = 1/10$ . Row 2: (d) - (f) prisms assigned negative polarity: (d)  $T/L = 1/50$ ,*  
 10 *(e)  $T/L = 1/25$ , (f)  $T/L = 1/10$ . (g) apolar  $T/L = 1/5$  prism. (h) The same capillary-driven*  
 11 *binding states are observed at air-gellan/water interface prior to prism immobilization as*  
 12 *are observed with optical microscopy at non-gelled interfaces. Scale bars are  $20 \mu\text{m}$ .*

13 Interface attachment of the  $T/L = 1/25$  prisms are shown in Figure 5b and e. The  
 14 top face of a prism in Figure 5e is covered by the gelled interface (as evidenced by the  
 15 rippling texture on top of this prism, which is consistent with the surface of the gelled

1 water phase elsewhere in the image), while several other prisms in the image sit with  
2 their top faces uncovered by the interface (as evidenced by the smooth texture of the  
3 exposed faces of these prisms, relative to the rippling surface of the gelled water phase).  
4 The  $T/L = 1/25$  prisms do not appear as bowed as the  $T/L = 1/50$  prisms. Still, evidence  
5 for polarity in prism-interface attachment is apparent because the covered prisms' centers  
6 of mass sit below the interface (in the gelled water phase), and the uncovered prisms'  
7 centers of mass sit above the interface (in the air phase). Polarity is again observed for  
8  $T/L = 1/10$  prisms, shown in Figure 5c and f. Several prisms rest with their centers of  
9 mass below the interface, and the top face of the prism is covered by the surface of the  
10 gelled interface, while other prisms sit substantially higher on the interface, with their top  
11 faces exposed to the air phase. Polarity of the prism position relative to the interface is  
12 not apparent for  $T/L = 1/5$  prisms. Fig. 5g is representative of all observed  $T/L = 1/5$   
13 prisms; the interface is observed to rise at the corners of the prisms, and prisms all appear  
14 to sit at the same interface position, relative to both the interface and to one another.

15 The optical micrographs also show evidence for bowing in  $T/L = 1/50$  (Fig. 4a)  
16 and  $1/25$  (Fig. 4b) prisms. That is, prisms of assigned polarity appear to have bright,  
17 central bodies and dark tips when prisms reside on the same side of the interface as the  
18 focal plane, and faded central bodies and bright tips when they reside on the opposite side  
19 of the interface as the prisms. This illumination contrast appears consistent with a  
20 difference in the position of the prism central body and tips relative to the microscope's  
21 focal plane. Moreover, referring back to Figure , bowing is apparent in the SEM images  
22 of the prisms as originally fabricated. Apparently, this bowing is a permanent,  
23 reproducible feature of the thin prism fabrication; it persists from synthesis to assembly.

24 Bowing can specify the curvature of the interface at the prism boundary by  
25 contact line pinning. This interfacial curvature in turn determines the capillary-driven  
26 attraction between the prisms. Figure 5 show that prisms with positive polarity (on top of  
27 the interface) are bowed downwards (with tips pointing towards the water phase), and  
28 negative polarity (below the interface) prisms are bowed upwards (with tips pointing  
29 towards the air phase). In both cases, the interface appears pinned to the corner of the  
30 prism's edge and to the concave face. Thus, the curvature of the interface follows the  
31 curvature of the bowed prism. The result is that the interface curvature at the tips and  
32 edges of triangle is opposite for prisms of positive and negative polarity.

33 Inhomogeneity in prism surface wetting – which could potentially be introduced  
34 during prism fabrication as described in the methods – is not the source of prism polarity.  
35 Thin prisms ( $T/L \leq 1/10$ ) fabricated with or without plasma treatment on one side each  
36 exhibit the two polarity states. The plasma treatment affects wetting; the contact angle  
37 change in the plasma treated prisms is  $\sim 70^\circ$  immediately following treatment. This  
38 insensitivity to plasma treatment supports the hypothesis that prism bowing is the primary  
39 driver of the observed polarity.

#### 40 *Correlation between prism interface polarity and bonding state*

41 The correlation between prism polarity (up or down interface attachment) and  
42 bonding state is examined for  $T/L = 1/50$  prisms in Figure ; Comparable measurements  
43 for  $T/L = 1/25$  are available in SI Figure 3. Each row of Figure shows one 1270 x 1270

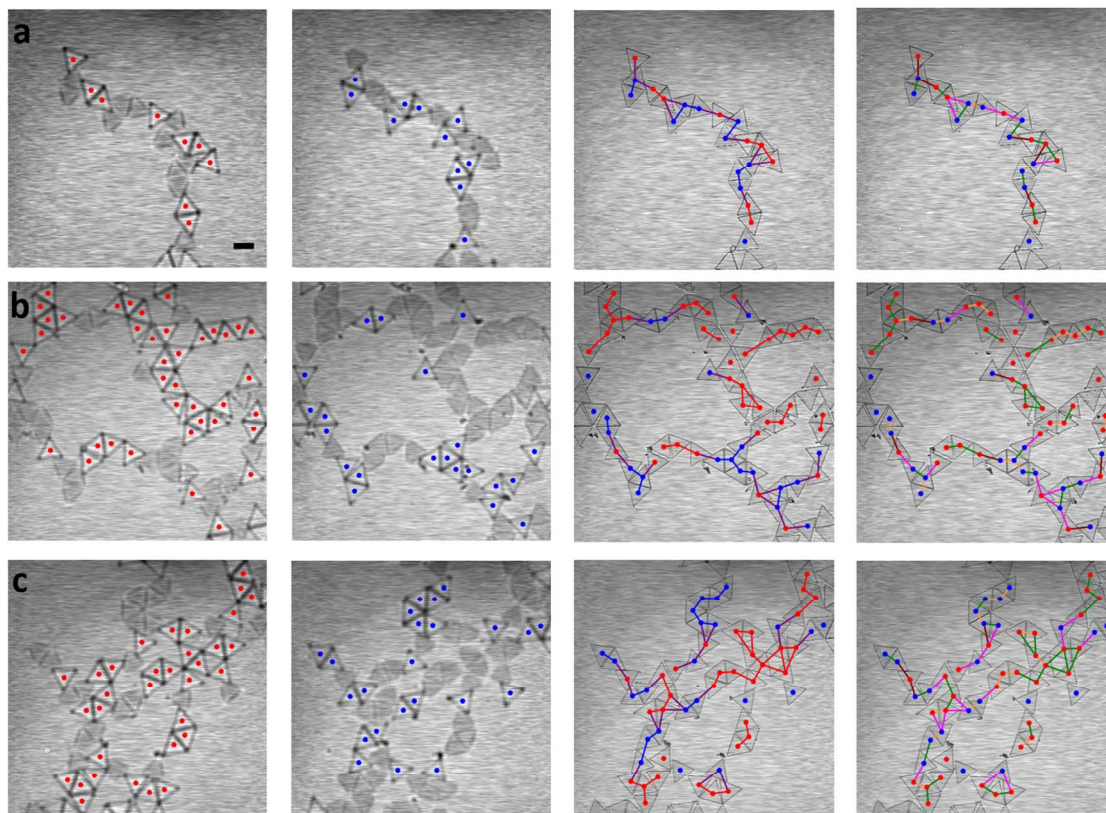
1  $\mu\text{m}$  region of an open network. In the first column, the focal-plane is located above the  
2 interface. In the second column, the focal-plane is located below the interface. In these  
3 first two columns, each prism is assigned a polarity, determined by the location of the  
4 prism center-of-mass, as described in the previous section. For  $T/L = 1/25$ , a polarity is  
5 assignable to all prisms.

6 In the third and fourth column, the focal-plane is located at the interface. In the  
7 third column, bonds between prisms with (a) the same polarity (identified with red and  
8 blue connecting lines for bonds between pair-bonded prisms of negative and positive  
9 polarity, respectively) (b) the opposite polarity (purple connecting lines), and (c)  
10 indeterminate polarity (black connecting lines) are predicted. In the fourth column,  
11 prism-prism bonds are measured by the relative orientation of the two prisms,  
12 independent of the polarity state of each prism. Four types of bonds are observed: (a) tip-  
13 tip (green connecting lines), (b) tip-edge (pink connecting lines), (c) edge-edge (orange  
14 connecting lines; edges of triangles are in registry – in contact and flush with one  
15 another), and (d) edge-edge offset (brown connecting lines; half of the edge of each  
16 bonded triangles lie flush with one another, with the tip of one triangle located at the  
17 center of the other triangle's edge).

18 Comparison of the predicted and measured bonded states for  $T/L = 1/25$  and  $T/L$   
19  $= 1/50$  prisms shows perfect correlation between the polarity states of any two adjacent  
20 prisms and their bonded state. Specifically, of all prisms whose polarity could be  
21 determined, all bonding between same polarity prisms is tip-tip or edge-edge, and all  
22 bonding between opposite polarity prisms is tip-edge or edge-edge offset. The bonded  
23 states – both measured and predicted based on polarity – are available in SI Tables 1 ( $T/L$   
24  $= 1/25$ ) and 2 ( $T/L = 1/50$ ).

25

26



1

2 *Figure 6 Identification of triangular prism binding states ( $T/L = 1/25$ ). Each row of images*  
 3 *(a) – (c) represents a different location within a network structure. The relative position*  
 4 *of microscope's focal plane to the air-water interface is varied by column as follows:*  
 5 *Column (1): Microscope focal plane is  $\sim 200 \mu\text{m}$  below the interface. Clearly visible*  
 6 *prisms are identified with red markers. Column (2): Microscope focal plane is  $\sim 200 \mu\text{m}$*   
 7 *above the interface. Clearly visible prisms are identified with blue markers. Column (3):*  
 8 *Microscope focal plane is at the interface. Bonds between prisms with the same polarity*  
 9 *are identified with blue and red connecting lines, bonds between prisms with the opposite*  
 10 *polarity are identified with purple connecting lines. Column (4): Microscope focal plane*  
 11 *is at the interface. Prism-prism bonds are identified by their polarity-independent*  
 12 *orientation: side-side (orange connecting lines), tip-tip (green connecting lines), side-*  
 13 *side offset (brown connecting lines), tip-side (pink connecting lines). Bonds in Columns*  
 14 *(3) and (4) are tabulated in Table (S1). Scale-bar is  $100 \mu\text{m}$ .*

15 *Theoretical analysis and computation of capillary interactions of triangular prisms*

16 The triangular prisms in these experiments have flat, nearly vertical side surfaces.  
 17 This lack of curvature of the prism sides leads to a different kind of interface attachment  
 18 than that observed with ellipsoids and cylinders. As discussed in <sup>11–13,41</sup>, interfaces  
 19 around the ellipsoids and cylinders either rise or fall as a result of variations in curvature  
 20 of the side surface of the prism. A constant contact angle as well as zero total force and  
 21 torque on an isolated prism is maintained.

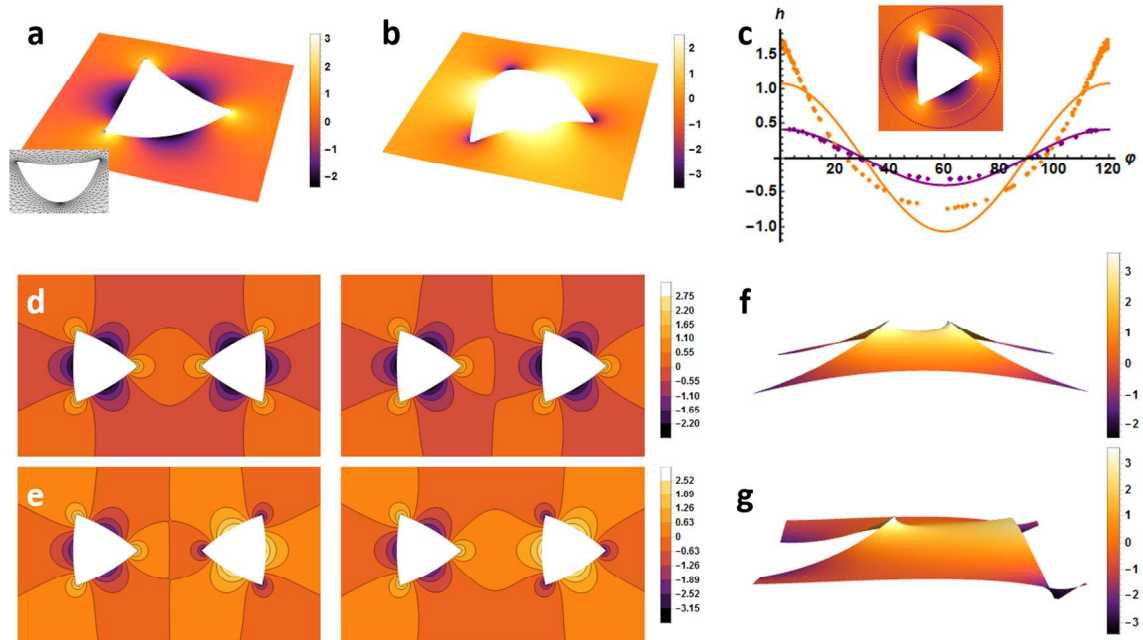


Figure 7 Interface height profile for (a) negative polarity bowed-up triangular prism and (b) positive polarity bowed-down triangular prism, where the zero value is set by the equilibrium interface height at large distances from the prism. The inset in (a) is a close-up of the Surface Evolver simulation output. (c) A comparison of the interface height profile around a bowed-up triangular prism (data points) and an ideal hexapole (solid curves) as a function of angle at two different distances from the triangular prism, shown in the inset. Simulated interface height profiles for (d) two bowed-up triangular prisms and (e) one bowed-up and one bowed-down prism for both tip-to-tip and tip-to-side configurations. Zoomed-in rendering of simulated interface height profile for (f) a tip-to-tip configuration for two bowed-up prisms; and (g) a tip-to-side configuration for one bowed-up and one bowed-down prisms, illustrating the existence of a capillary bridge in both cases.

1 For these triangular prisms with vertical side surfaces, however, the preferred  
 2 contact angle ( $\sim 5$  degrees) of the material cannot be reached, because it would  
 3 correspond to a uniform rise of the interface around the triangular prism, yielding a net  
 4 force pointing down on the prism; this net force is inconsistent with mechanical  
 5 equilibrium. Therefore, instead of an equilibrium contact line in the middle of the side  
 6 surface of the triangular prisms, the interface is pinned to the edges of the concave face of  
 7 the triangular prisms with a non-equilibrium contact angle that satisfies mechanical  
 8 equilibrium (see Supplementary Information for further discussion of this phenomenon).  
 9 Contact-line pinning has been observed in various experimental systems consisting of  
 10 solid prisms or substrates containing sharp edges.<sup>42–45</sup>

11 To characterize the interface shape and the resulting capillary interaction between  
 12 the triangular prisms, we use Surface Evolver to compute the interface with a contact line  
 13 pinned to the edges of a bowed triangle (for details see the Materials & Methods section).  
 14 To match the observed curvature of the thinnest prisms, we use an inverse-curvature-to-  
 15 edge-length ratio of 0.9 (that is, for an edge length of  $120 \mu\text{m}$ , we take the radius of  
 16 curvature to be  $108 \mu\text{m}$ ). The resulting interface around isolated prisms (Figure 7a,b)  
 17 closely resembles that observed in the eSEM images of the thinnest prisms (Figure 5a,d).

18 It is worth noting that the only input into the Surface Evolver computation is the  
 19 pinned contact line, and no information about the prism thickness is involved. Our  
 20 computation shows that, for a bowed-up prism (Figure 7a), the prism center of mass is

1 below the interface in the far field by  $7.45 \mu\text{m}$  (for the given curvature), whereas the  
 2 center of mass of a bowed-down prism is the same amount above the far-field interface.  
 3 This depth is greater than the prism thickness, and explains the perfect correlation  
 4 between the polarity and the direction of the prism bowing of the thinnest prisms. (The  
 5 relation between the interface attachment and the bowing direction of the thicker prisms  
 6 may involve mechanisms such as variability in interface height due to roughness and  
 7 interface pinning; these mechanisms lead to weak quadrupolar interactions, as described  
 8 in ref. <sup>46 46</sup>).

9 The interface geometry around the triangular prisms is similar to that of the  
 10 capillary hexapole (discussed in detail in Supplementary Information) in that there are six  
 11 regions of alternating positive- and negative-interface heights (where the equilibrium,  
 12 unperturbed height of the interface at far distances is taken to be zero). However,  
 13 important differences exist between the ideal hexapole field and the interface around the  
 14 triangular prisms at distances close to the prism. The ideal hexapole field with height  
 15  $h \sim \frac{1}{r^3} \cos 3\theta$ , has the symmetry that the positive and negative regions are of equal width.  
 16 The interface around the triangular prisms, in contrast, has much narrower positive  
 17 (negative) regions around the tip of the bowed-up (-down) triangles (Figure 7c). As a  
 18 result, the focusing of excess area around the tips of the triangles induces stronger  
 19 capillary interactions at the tips than along the triangle edges. Note that, as one would  
 20 expect, the height of the interface around a bowed triangular prism increasingly conforms  
 21 to the profile of a capillary hexapole as the distance from the prism increases. Indeed, the  
 22 effect of tips, edges, and other sharp prism features, which are quite prominent in the  
 23 near-field behavior of the interface, becomes increasingly diminished and smoothed out  
 24 at these larger distances (Figure 7c).

25 We study the capillary interaction potential between triangular prisms by  
 26 computing the interface geometry around a pair of triangular prisms using Surface  
 27 Evolver. Once the numerical interface solution has been obtained, we can subsequently  
 28 determine the capillary interaction energy using  $U_{12} = \gamma(\delta S_{12} - \delta S_1 - \delta S_2)$ , where  $\gamma$  is  
 29 the air-water surface tension,  $\delta S_{12}$  is the excess area created at the interface in the full  
 30 two-prism system, and  $\delta S_i$  ( $i = 1,2$ ) is the excess area in an isolated one-prism system  
 31 (i.e., for separation distance  $r \rightarrow \infty$ ). The excess area is defined as the difference between  
 32 the actual surface area  $\Sigma^*$  and the projected surface area  $\Sigma$  (see Supplementary  
 33 Information). There are, of course, two cases to be simulated: the first is when both  
 34 prisms have the same bowing polarity (by symmetry, we need only consider the case  
 35 where both prisms are bowed up), and the second is when the two prisms have opposite  
 36 polarities (here again we can simplify matters and consider only the case where the prism  
 37 on the left is bowed up and the prism on the right is bowed down). Examples of the  
 38 interface in the vicinity of two triangular prisms with the same and opposite polarities are  
 39 shown in Figure 7d,e.

40 It is already evident from these plots – even before further analysis – that the tip-  
 41 tip configuration for prisms with the same polarity and the tip-edge configuration for  
 42 prisms with opposite polarities are attractive, while the opposite configurations are  
 43 repulsive – the former will result in decreased excess area as the prisms move towards  
 44 each other, while the latter will result in increased excess area (the overall slope of the

1 interface will increase between the bowed-up and bowed-down components as they are  
 2 brought closer together). Figure 7f,g show the underlying mechanism that reduces the  
 3 excess area between regions with the same capillary charge: the formation of a capillary  
 4 bridge.

5 The capillary interaction potential  $U$  depends on both the distance between the  
 6 centers of the two triangular prisms,  $r$  and their orientations relative to the line  
 7 connecting their centers,  $\theta_1, \theta_2$  (Figure ). This is a configuration space that has one extra

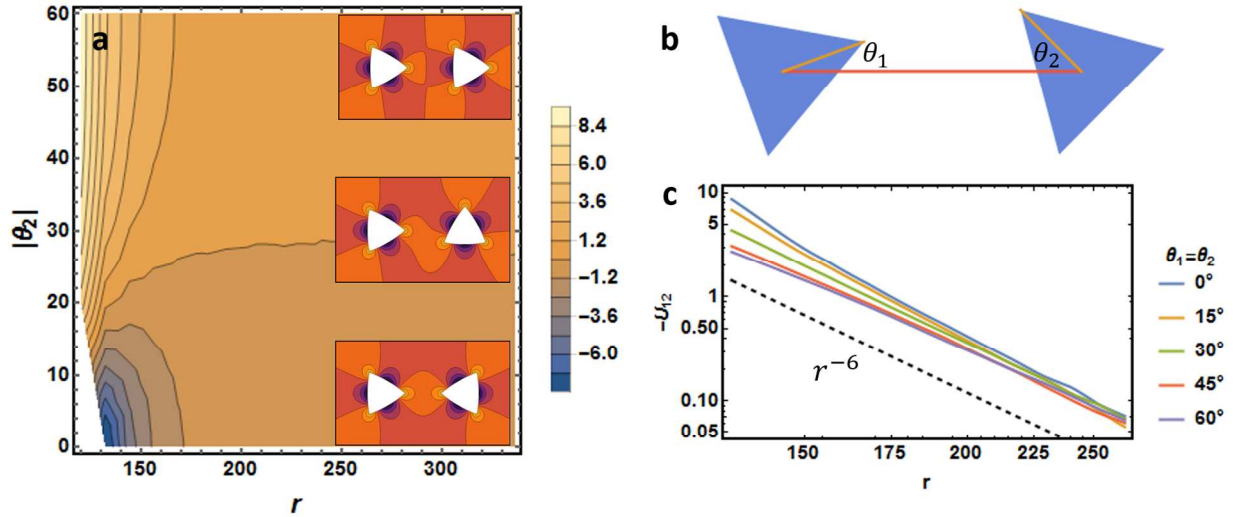


Figure 8 Numerically-simulated capillary interaction potential between two bowed-up triangular prisms, with the left prism held at  $0^\circ$ . This two-dimensional slice of the full three-dimensional configuration space is directly comparable to the theoretical interaction potential in Figure S2. (b) All orientation angles for the triangular prism system are defined according to the convention shown: the orientations are defined by the angle a specific tip of the prism makes with the line connecting the centers of the two prisms. (c) The capillary interaction potential for two-bowed up triangular prisms in mirror-symmetric configurations as a function of the separation distance,  $r$ , on a log scale, for various orientation angle values. A dashed reference line, corresponding to the theoretical interaction potential for two ideal hexapoles,  $U \sim r^{-6}$ , is shown for comparison.

8 dimension beyond that of the capillary hexapolar theory discussed in Supplementary  
 9 Information, in which only the relative orientation of the two prisms matters. In order to  
 10 be able to directly compare the theoretical case with that of two bowed-up triangular  
 11 prisms, we fix the orientation of the left prism to be  $0^\circ$  and allow  $r$  and  $\theta_2$  to vary. The  
 12 resultant potential, shown in Figure a, is very similar to that of the ideal hexapoles; even  
 13 the general shapes of the interfaces, as shown in a few select cases as insets in both plots,  
 14 share similar features.

15 The similarities extend beyond this, as well: in Figure , when comparing potential  
 16 curves for various mirror-symmetric configurations in the triangular-prisms system with  
 17 that of the mirror-symmetric curve in the ideal-hexapoles system, which has a  $r^{-6}$   
 18 dependence, we see that all the curves approach the theoretical ideal-hexapole curve at  
 19 long distances, as we expect from the interface profile. Deviations from the ideal-  
 20 hexapole curve and from each other occur at short inter-prism distances, where the  
 21 anisotropic tips become increasingly prominent. Note that the  $\theta_1 = \theta_2 = 0^\circ$  tip-tip mirror  
 22 symmetric configuration is favored for these smaller distances.

- 1 This deviation from an ideal hexapole is further portrayed in Figure . In the case of ideal  
 2 hexapoles, since the interaction energy depends only on the relative orientations of the

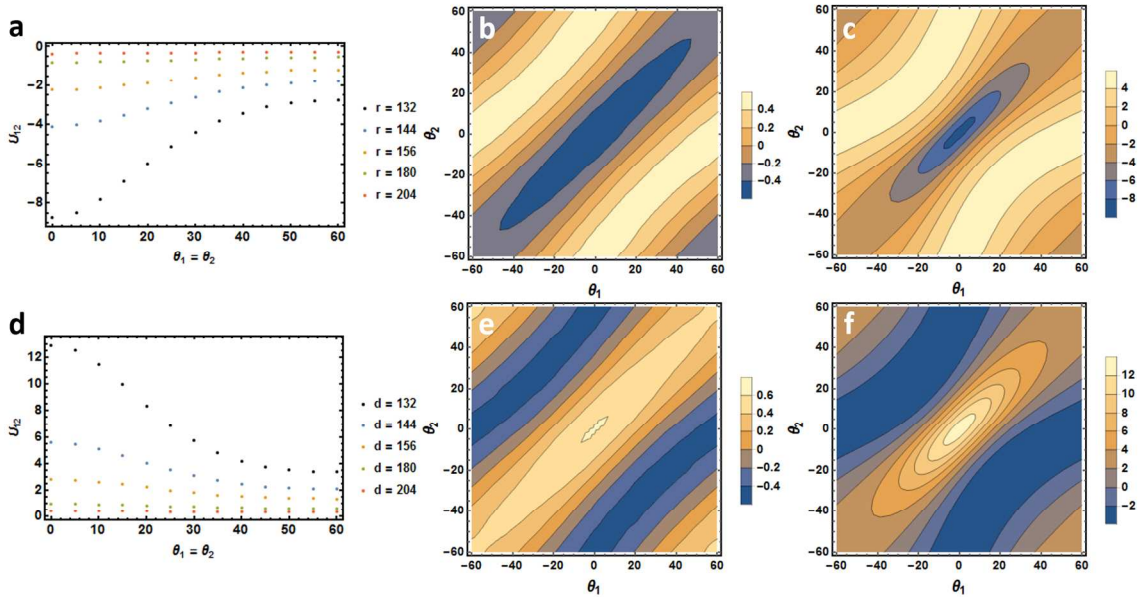


Figure 9 (a) Interaction energy potential values for two bowed-up triangular prisms in mirror-symmetric configurations at various separation distances.  $0^\circ$  corresponds to a tip-to-tip configuration, while  $60^\circ$  corresponds to a side-to-side configuration. Interaction energy potentials plotted as a function of orientation angles for (b)  $r = 192 \mu\text{m}$  and (c)  $r = 132 \mu\text{m}$ . (d)-(f) The corresponding three figures for the case of one bowed-up and one bowed-down triangular prism.

- 3 prisms, the interaction energy for all mirror symmetric configurations, in which  $\theta_1 = \theta_2$ ,  
 4 for a given distance is perfectly degenerate. As shown in Figure 9a,d, for the system of  
 5 triangular prisms, however, the tip-tip mirror symmetric configuration (corresponding to  
 6  $\theta_1 = \theta_2 = 0^\circ$ ) is strongly favored (disfavored) compared to the edge-edge mirror  
 7 symmetric configuration (corresponding to  $\theta_1 = \theta_2 = 60^\circ$ ) for smaller values of inter-  
 8 prism distances,  $r$  in the same- (opposite-) polarities system. In the case of opposite  
 9 polarities, even though the edge-edge configuration is preferred over the tip-tip  
 10 configuration, it is important to realize that it is *not* the global preferred state, which is a  
 11 non-mirror-symmetric configuration, as will be discussed further subsequently. Once  
 12 again, in both cases, the expected ideal-hexapole behavior of degenerate energies for all  
 13 mirror symmetric configurations is recovered as the inter-prism distance is increased.

- 14 As shown in Figure 9b,c, the potential for a pair of bowed-up triangular prisms  
 15 shows a clear well for the mirror symmetric configuration,  $\theta_1 = \theta_2$ , which becomes  
 16 increasingly deep for smaller inter-prism distances. It is clear in Figure 9b, as well,  
 17 that for two bowed-up triangular prisms, the potential is relatively flat for all mirror  
 18 symmetric configurations at a given large distance (same as ideal hexapole interaction).  
 19 However, when the two prisms are close, the tip-to-tip configuration is much more  
 20 preferred (in contrast to the ideal hexapole). The above results indicate that when two  
 21 bowed up prisms approach one another, in general, they first rotate into mirror symmetric  
 22 configurations, and then rotate to tip-to-tip when they are very close to each other. The  
 23 case of two bowed-down triangular prisms is very similar to the discussion above for the

1 bowed-up case, with the simple addition of a minus sign of the interface height, which  
2 results in the same interface energy.

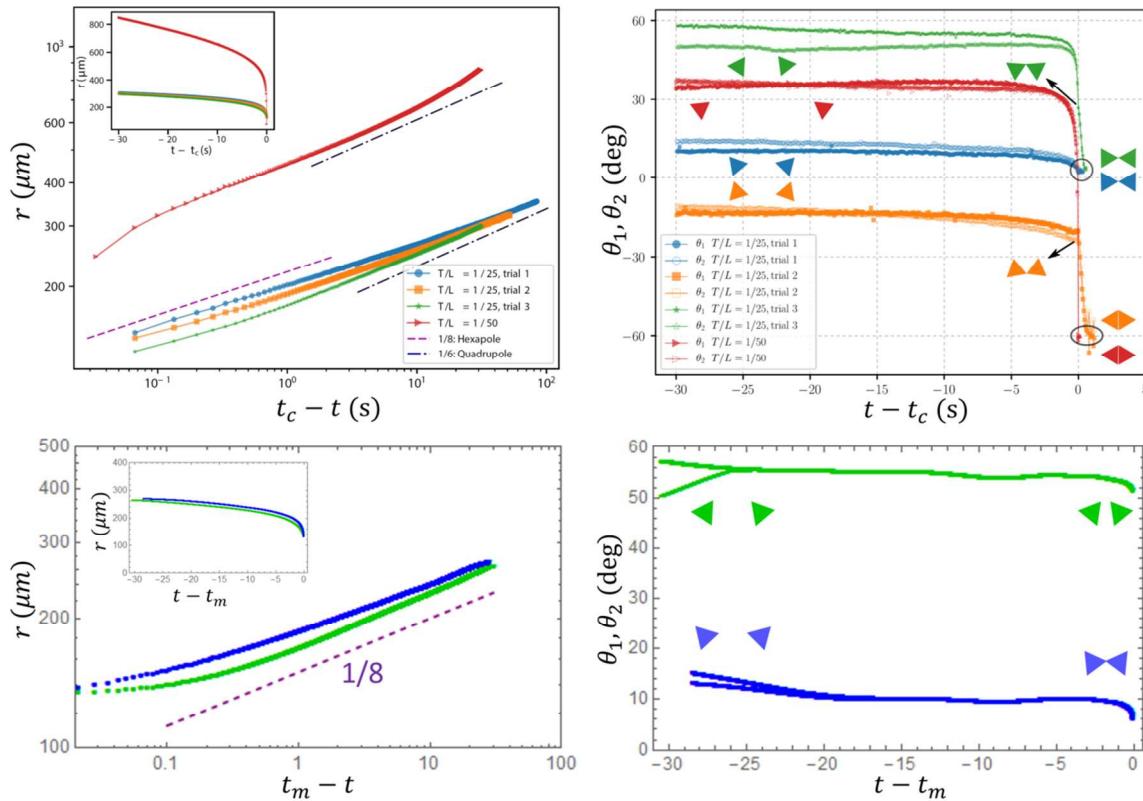
3 The case of one bowed-up triangular prism and one bowed-down triangular prism  
4 is quite different. At large distances, the capillary interaction is close to that between two  
5 hexapoles but with one hexapole rotated by  $60^\circ$  degrees (or equivalently the “+” and “-”  
6 capillary charges switched). Interestingly, at small distances, the potential energy valley  
7 appears curved in  $(\theta_1, \theta_2)$  space while slightly favoring offset edge-edge configuration  
8 (Figure 9e). As we see below, this leads to different binding trajectories for bowed-up  
9 pairs and up-down pairs.

### 10 *Dilute binding events: experimental observations*

11 In order to evaluate the modeling of the capillary interaction between the  
12 triangular prisms, we simulate pair trajectories of prisms from various initial conditions,  
13 and compare these trajectories with trajectories observed in experiments. The centroidal  
14 separations,  $r$ , and angular orientations of the two prisms relative  $\theta_1$  and  $\theta_2$  were collected  
15 by image analysis. The trajectories are available in Movies S1 through S7. SI Figure  
16 4a,b,c, and d show frames from the trajectories from Movies S1, S2, S4 and S7,  
17 respectively.

18 Seven trajectories (five for  $T/L = 1/25$  and two for  $T/L = 1/50$ ) were collected  
19 from the SI movies; separations and orientations are reported in Figures 10 and 11. Four  
20 of the trajectories report like polarity binding (c.f. Fig. 10). Three trajectories report  
21 opposite polarity binding (c.f. Fig. 11). Qualitative features observed for dilute binding  
22 trajectories are: (i) like polarity prisms, in a first stage adopt mirror symmetric  
23 configurations and slowly move toward each other; in a second stage, prisms rapidly  
24 close into a tip-tip binding; and in a third stage, some prisms then rotate into a edge-edge  
25 configuration; (ii) opposite polarity prisms approach to a tip-midpoint edge configuration;  
26 the pair finally collapses into an offset edge-edge bond.

27 Figure also shows that the time for binding of  $T/L = 1/50$  prisms is significantly  
28 faster than for  $T/L = 1/25$  prisms. This difference indicates that capillary attractions are  
29 much stronger at separation distances of up to several prism edge lengths for  $T/L = 1/50$   
30 prisms as compared to  $T/L = 1/25$  prisms. By contrast, there is negligible difference in  
31 the time scale of tip-tip and tip-edge binding at fixed  $T/L$  ratio, an indication that the  
32 strength of like-polarity and opposite-polarity interactions are similar. Furthermore, the  
33 exponent associated with prisms approaching each other in these binding events,  
34  $\sim(t_c - t)^\beta$ , where  $t_c$  is the time of contact, defined as the first image frame where the  
35 two prisms touch, displays similarity with the exponent from hexapole-hexapole  
36 interactions,  $\beta_0 = 1/8$  (Figure ). The small deviation comes from the difference between  
37 the actual capillary interactions between the triangles with the ideal hexapolar interaction.  
38 In particular, at far distances,  $\beta$  appears to be closer to  $1/6$ , indicating that at far-field  
39 quadrupolar interactions (from random variations in prism edge topography) may be the  
40 dominant driver for binding at these large separations. Nevertheless, the scaling at small  
41 separation approaches the hexapolar expectation of  $1/8$ .



1

2 *Figure 10 Comparison of experimentally observed and simulated trajectories for a pair of prisms of same polarity.*  
 3 *Top row: observed  $r$  vs  $t_c - t$  curve in log-log scale (left) and linear scale (inset), where  $t_c$  is taken to be the first*  
 4 *frame in which the two prisms touch; and observed  $\theta_1, \theta_2$  vs  $t - t_c$  curves (right). Four events are shown as*  
 5 *explained in the legend, and lines showing  $\beta = 1/8$  (consistent with hexapolar interaction) and  $1/6$  (consistent*  
 6 *with quadrupolar interaction) are added. Illustrations of the prisms configurations are added in the  $\theta_1, \theta_2$  plot to*  
 7 *show the geometry. Configurations at the time of contact ( $t = t_c$ ) are pointed to by arrows, and the points at*  
 8  *$t - t_c > 0$  show prism rotations after contact, with final configurations marked by circles. Bottom row:*  
 9 *counterparts of the  $r$  and  $\theta_1, \theta_2$  plots from simulation. Instead of contact time,  $t_m$  is the time where the prisms'*  
 10 *separation distance reaches  $r_m = 132 \mu\text{m}$  (the lower bound of  $r$  in our computation), at which they touch if*  
 11  *$\theta_1 = \theta_2 = 0$ . We have chosen initial conditions that are close to two experimental trajectories.*

12 Turning to prism rotation, for tip-to-tip trajectories, prism rotation begins between  
 13 hundredths of a second ( $T/L = 1/25$ ) up to several seconds ( $T/L = 1/50$ ) prior to contact  
 14 (Fig. 10). In the later case, these times correspond to separation distances that are several  
 15 edge lengths. The angular orientation plots also show that prisms bind in a mirror  
 16 symmetric fashion; that is, in each pair-binding event, both prisms rotate an equal amount  
 17 into their final, steady-state orientation. For tip-to-midpoint edge trajectories, prism  
 18 angular orientation also begins at distances corresponding to separations of several edge  
 19 lengths (Fig. 11).

20

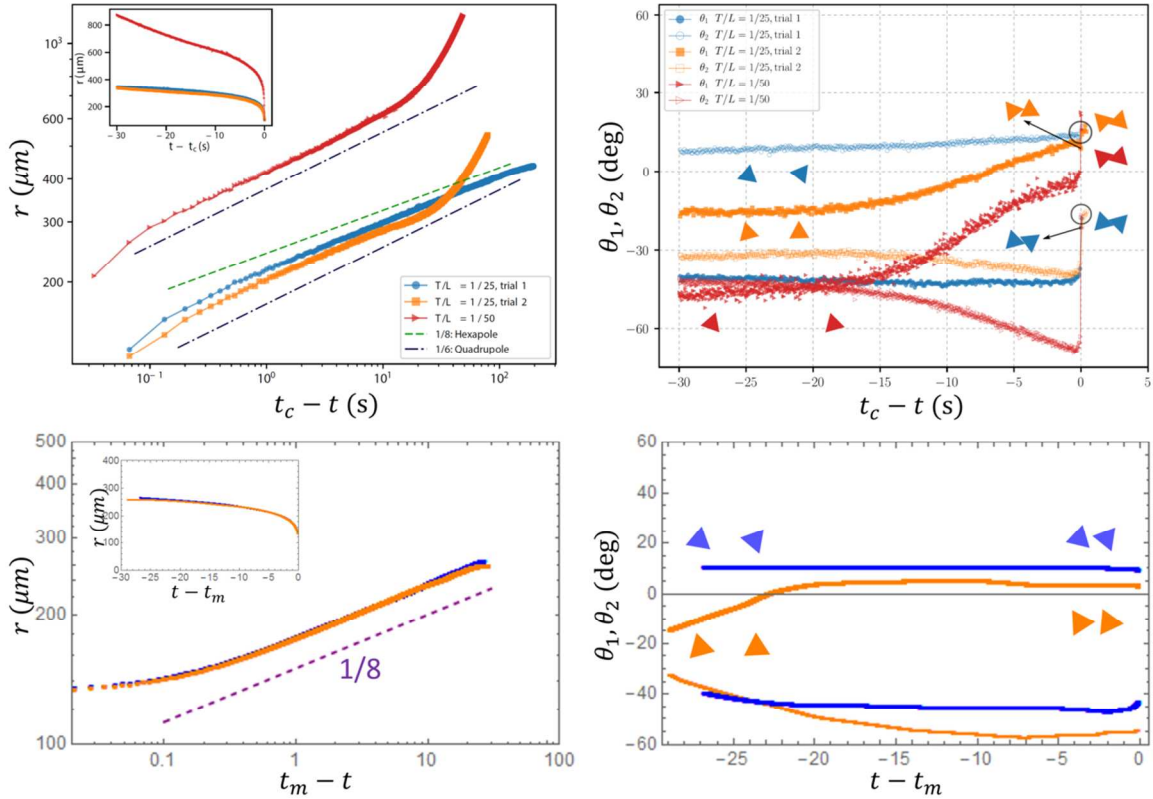


Figure 11 Comparison of experimentally observed and simulated trajectories for a pair of prisms of opposite polarity. Top row: experimental observations. Bottom row: simulation results. All conventions are the same as in Figure . Note that in two experimental events, the prisms approach faster in the far-field regime than quadrupolar interactions would dictate; we speculate that this is due to noncapillary-induced drift of particles at the interface, possibly owing to convective flow at the interface surface .

### 1 Dilute binding events: simulation results and agreement with experiments

2 To compare to these results, we simulated pair-binding events using the  
 3 interaction potential (interface energy)  $U(\theta_1, \theta_2, r)$  obtained by interpolating a grid of  
 4 Surface Evolver-calculated potential values at regular intervals as described above.  
 5 Details of the trajectories simulation are described in the Materials & Methods section.

6 Examples of our simulation results for same-polarity (both bowed up in our  
 7 calculation) and opposite-polarity prisms are shown in Figures 12 and 13, respectively.  
 8 Initial conditions were chosen to approximate trajectories observed experimentally. The  
 9 ratio of the two viscous-damping coefficients is taken to be  $\eta_{\bar{\theta}}/\eta_r = 1.46$  as discussed in  
 10 Materials & Methods, and  $\eta_r$  is taken to rescale time such that the arbitrary time scale in  
 11 the simulation approximates the experimental time scale, in units of seconds. These  
 12 simulations terminate at  $r_m = 132 \mu\text{m}$ , the distance at which the two prisms would touch  
 13 if they faced one another tip-to-tip. In all cases, the far-field trajectories are roughly  
 14 consistent with that of the ideal hexapole-hexapole interaction, while expected, and  
 15 important, deviations from the ideal interaction occur as the separation distance  
 16 decreases. In Supplementary Information we show additional trajectories where  
 17 additional initial conditions with different choices of  $\eta_{\bar{\theta}}/\eta_r$  ratio are discussed.

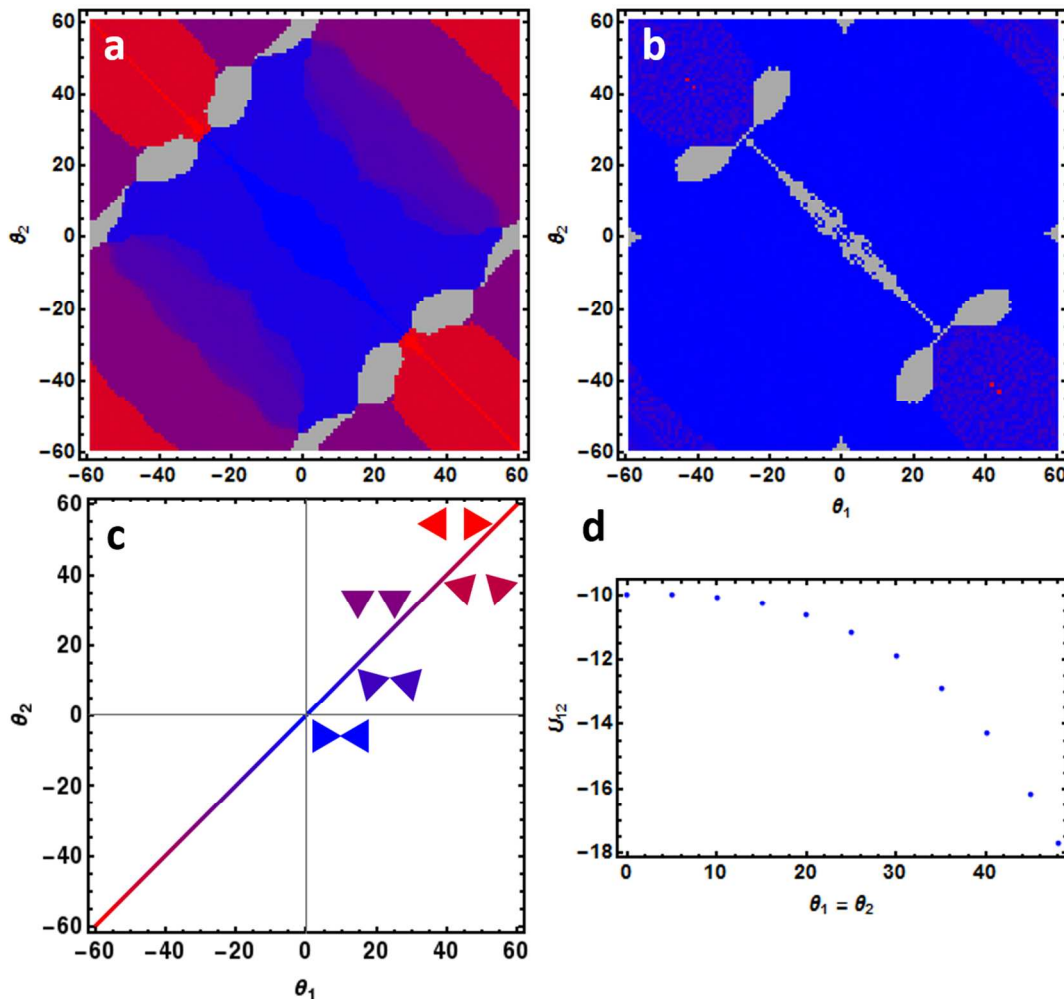


Figure 12 “Phase” diagrams illustrating the final configurations ( $r = 132 \mu\text{m}$ ) for all possible initial orientations for two bowed-up triangular prisms at  $r = 264 \mu\text{m}$  for two different viscous-damping coefficient ratios, (a)  $\eta_b/\eta_r = 1.46 (\mu\text{m}/^\circ)^2$  and (b)  $\eta_b/\eta_r = 0.146 (\mu\text{m}/^\circ)^2$ . The final configurations are all mirror-symmetric and lie somewhere along the line in (c), with blue corresponding to tip-to-tip final configurations, red corresponding to side-to-side final configurations, and gray denoting initial conditions that lead to trapped configurations due to numerical artifacts in the computed pair potential. (d) Capillary interaction potential values for mirror-symmetric configurations with two tips of the triangular prisms remaining in contact (thus, the separation distance,  $r$ , decreases below  $132 \mu\text{m}$  as  $\theta_1 = \theta_2$  increases). Indicates a tendency for tip-to-tip configurations to ultimately collapse to side-to-side configurations.

- 1 To obtain statistics about how the triangular prisms bind, we ran simulations for all

1 initial angles of prism pairs at an initial distance of  $r_0 = 264 \mu\text{m}$ ; our results are  
 2 summarized, for two different ratio values,  $\eta_{\bar{\theta}}/\eta_r = 1.46 (\mu\text{m}/^\circ)^2$  and  $0.146 (\mu\text{m}/^\circ)^2$ ,  
 3 in Figure 12a,b. The first ratio is chosen according to the simple geometric estimate  
 4 discussed previously. The second ratio, which is 10 times smaller, allows the prisms to  
 5 rotate faster relative to their center of mass motion, and presents a useful contrast to the  
 6 first case. In both cases, a significant majority of configurations end up in, or close to,  
 7 the  $\theta_1 = \theta_2 = 0^\circ$  tip-tip mirror-symmetric configuration. For the case of  $\eta_{\bar{\theta}}/\eta_r =$   
 8  $1.46 (\mu\text{m}/^\circ)^2$ , some trajectories end up along a continuum of mirror symmetric  
 9 configurations ranging from tip-to-tip to edge-to-edge, as the prisms did not have enough  
 10 time to finish the rotation before contact. Contrastingly, in the second case with  $\eta_{\bar{\theta}}/\eta_r =$   
 11  $0.146 (\mu\text{m}/^\circ)^2$  almost all trajectories end up tip-to-tip, because rotational drag is smaller,  
 12 leading to faster rotation. Note that the trajectory simulations are deterministic, as they  
 13 involve energy minimization in which the only relevant energy is due to the pairwise  
 14 capillary interaction; as discussed, this approach is consistent with the limits we are  
 15 considering, in which capillary interactions are dominant over all other (stochastic)  
 16 processes. Any slight fluctuations in the simulation results are due to small kinks in the  
 17 pair potential arising from the Surface Evolver simulations. In particular, a small fraction  
 18 of initial conditions (gray in the figure) ended up in random configurations.

19 In order to investigate what happens after the two prisms touch at their tips, we calculated  
 20 the pair potential for two prisms in which their tips continue to touch, but at different  
 21 orientations (mirror symmetric configurations with  $\theta_1 = \theta_2$  ranging between 0 and  $60^\circ$ ),  
 22 as shown in Figure 12d. This indicates that, after initial tip-to-tip contact, the pair of  
 23 triangular prisms will rotate and “collapse” into an edge-to-edge configuration. It is  
 24 worth pointing out that although – after collision – the prisms collapse into the edge-to-  
 25 edge configuration, a majority of trajectories still first go through an initial tip-tip  
 26 binding. This is in good agreement with our experimental observations.

27 For bowed-up-bowed-down pairs, a similar set of simulations yields results shown in  
 28 Figure 13a,b for the two viscous-damping coefficient ratios. In this case, it is important to  
 29 note that the final configurations are not mirror symmetric; Figure 13c shows the final  
 30 orientation values for the two triangular prisms. The curves of final orientation lie along  
 31 the minimum-energy regions of the opposite-polarity interaction potential in Figure 9f.

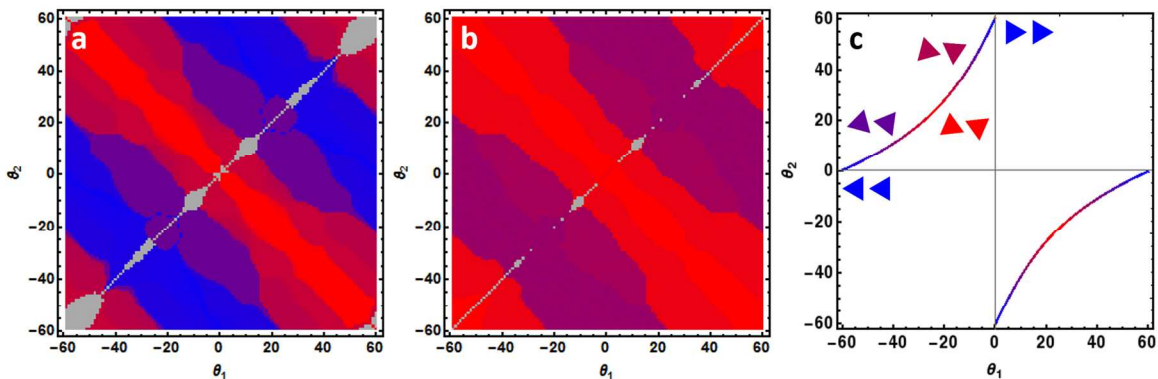


Figure 13 “Phase” diagrams illustrating the final configurations ( $r = 132 \mu\text{m}$ ) for all possible initial orientations for one bowed-up and one bowed-down triangular prism at  $r = 264 \mu\text{m}$  for two different viscous-damping coefficient ratios, (a)  $\eta_{\bar{\theta}}/\eta_r = 1.46 (\mu\text{m}/^\circ)^2$  and (b)  $\eta_{\bar{\theta}}/\eta_r = 0.146 (\mu\text{m}/^\circ)^2$ . The final configurations lie somewhere along the curve in (c), with blue corresponding to tip-to-edge final configurations and red corresponding to offset-edge-to-edge final configurations.

1 Similar to the case of prisms with the same polarity, simulating the approach of prisms of  
 2 opposite polarities with the smaller drag coefficient ratio,  $\eta_{\bar{\theta}}/\eta_r = 0.146 (\mu\text{m}/^\circ)^2$ , leads  
 3 to a more uniform state diagram wherein all initial conditions have enough time to rotate  
 4 to the offset edge-to-edge configuration, which is of lower energy. The first case – which  
 5 uses the ratio from our geometric estimation – yields a continuum of final configurations.  
 6 As before, our simulation terminates at  $r_m = 132 \mu\text{m}$ , which is the distance at which two  
 7 prisms touch when they face one another tip-to-tip. The opposite-polarity prisms,  
 8 however, being in non-tip-to-tip configurations, are not yet touching at this distance. Our  
 9 additional computations of the interface energy shows that, at smaller distances, the offset  
 10 edge-to-edge configurations exhibit lower energy, leading to the final collapsed offset  
 11 edge-to-edge configurations as observed in experiment.

### 12 *Assembly into open networks*

13 The pair-binding observations discussed above indicate that self-assembly of thin,  
 14 triangular prisms may result in 2D networks with both open (tip-tip and tip-edge pair-  
 15 binding orientations) and close-packed (edge-edge and edge-edge offset pair-binding  
 16 orientations) conformation. We characterize statistical signatures of the resulting  
 17 disordered networks for these prisms, which will guide future study aiming at obtaining  
 18 regular open networks.

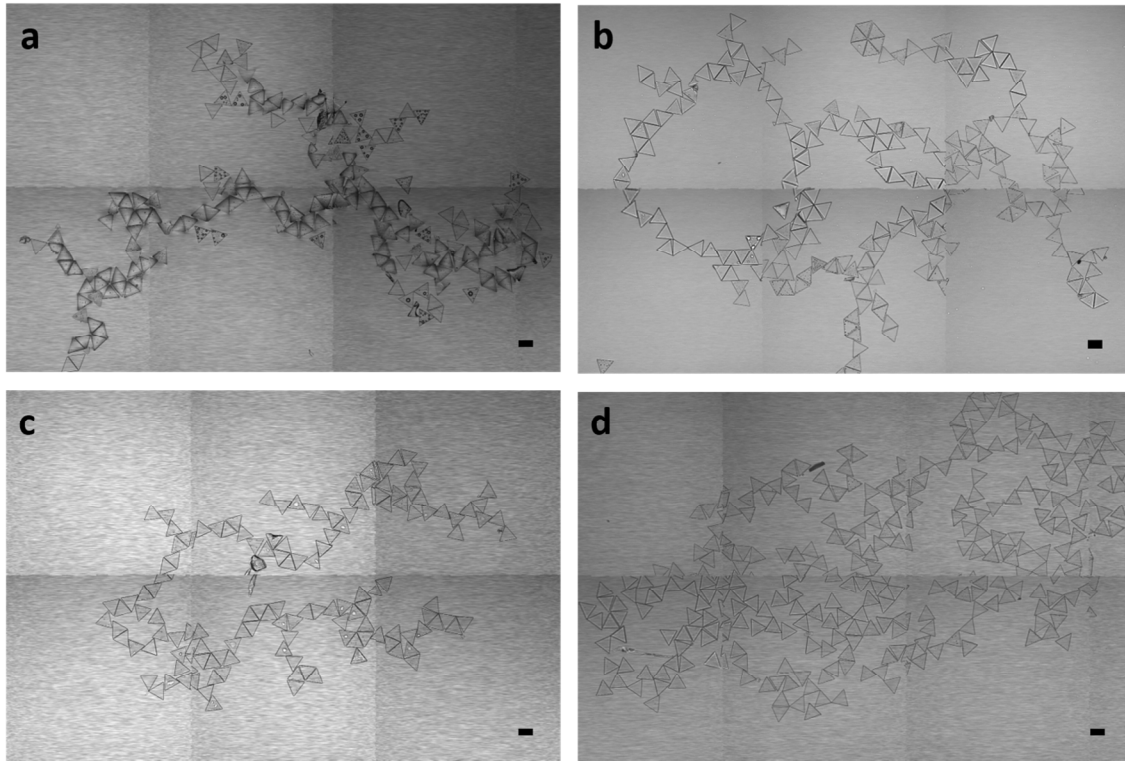
19 Recalling Fig. 3, at early times (Fig. 3b and c), small aggregates form. These  
 20 small aggregates undergo time-dependent growth via aggregate-aggregate attraction and  
 21 binding (Fig. 3d and e). These larger aggregates branch laterally, which yields an open  
 22 structure. Aggregates continue to attract and bind to one another until all available  
 23 prisms are incorporated into a space-spanning, open network. Representative networks  
 24 formed by self-assembly are shown for all T/L ratios in Fig. 14. Each of the four images  
 25 in Fig. 14 is a  $3.8 \times 2.5 \text{ mm}$  spatial mosaic of either six or eight (either three-by-two or  
 26 four-by-two)  $1270 \times 1270 \mu\text{m}^2$  microscopy images. While each of the self-assembled  
 27 networks possesses voids, the structures of the three thinnest prisms (T/L = 1/50, 1/25  
 28 and 1/10, which exhibit polarity) is comprised of long, nearly linear runs of triangles  
 29 bound in close-packed edge-edge states (Fig. 14a – c). By contrast, the thickest prisms  
 30 (T/L = 1/5, which do not exhibit polarity) contain fewer close-packed prisms, and no  
 31 linear chains of edge-edge bonds (Fig. 14d).

32 Network porosity is quantitatively assessed by computing a common measure of  
 33 number density fluctuations:

$$\chi_L = \frac{\langle N^2 \rangle - \langle N \rangle^2}{\langle N \rangle} \Big|_L$$

34 Here  $N$  is the number of prisms within an ensemble of square bins of size  $L$ . The  
 35 brackets denote the average over the ensemble. This quantity is equivalent to the  
 36 compressibility in the long wavelength limit; we here refer to it as  $\chi_L$ . The quantity  $\chi_L$   
 37 has previously been used to describe the long-range structure of colloidal gels.<sup>47–49</sup> The  
 38 network images in Fig. 10 were divided into square regions of  $240 \times 240 \mu\text{m}^2$ ,  $480 \times 480$   
 39  $\mu\text{m}^2$ , and  $720 \times 720 \mu\text{m}^2$  and the compressibility measure determined for each bin size;  
 40 the results are reported in SI Table 3. For each bin size, the compressibility measure is

1 greatest for the networks of the thinnest prisms (Figs. 14a-c), progressively decreasing for  
 2 the network of thicker prisms (Fig. 10d); this quantitative result is consistent with the  
 3 images in Figure 14, which show larger voids for the thin prism networks relative to the  
 4 thick networks.



5  
 6 *Figure 14 Self-assembled open networks from capillary-driven binding of thin triangular*  
 7 *microprisms. (a)  $T/L = 1/50$ , (b)  $T/L = 1/25$ , (c)  $T/L = 1/10$ , and (d)  $T/L = 1/5$  equilateral*  
 8 *triangular microprisms. Scale-bars are  $100 \mu\text{m}$ .*

## 9 Discussion

10 In the discussion that follows, we comment on the ramifications of the coupled  
 11 prism polarity and hexapolar-like interactions of the thinnest prisms. We address how the  
 12 polarity of pair-binding prisms is predicative of both pair-binding trajectories and of the  
 13 final pair-bonded state. We then discuss the effect of prism polarity on open network  
 14 structure and suggest a path to design a prism building block for an ordered kagome  
 15 lattice.

### 16 *Prism polarity is predictive of tip-tip vs. tip-edge binding trajectory*

17 The results show that for thin prisms ( $T/L = 1/25$  and  $1/50$ ) the type of prism-  
 18 prism bond formed may be predicted with 100% fidelity from the polarity of the two  
 19 prisms participating in the bonding event. Prisms of the same polarity only access the  
 20 tip-to-tip trajectory which then leads to the tip-tip and edge-edge final binding states,  
 21 while prisms of opposite polarity only access the tip-to-midpoint edge trajectory, which  
 22 then leads to tip-to-midpoint edge and edge-edge offset binding states. Our observations  
 23 suggest that the tip-tip and tip-edge binding states only survive at steady-state when the

1 collapse of the prisms into their edge-edge or edge-edge offset states is frustrated, due to,  
2 either geometrically induced frustration from surrounding prisms or roughness at the  
3 prism sides, which prevent rotations. Prism polarity – and its control over prism-prism  
4 binding trajectory – is also observed for  $T/L = 1/10$  prisms, although evidence of the  
5 effect is not as obvious with optical microscopy (Fig. 4c, columns 2 and 3) and thus was  
6 not analyzed in the same way thinner prisms are in Figs. 6 and S3.  $T/L = 1/5$  prisms, on  
7 the other hand, lack observable polarity. Fig. 4d shows a variety of bonding states along  
8 the edge – instead of localization at the tip and midpoint edge as seen for the thin prisms.

### 9 *Hexapole-like capillary interactions from interface-prism contact line bowing*

10 Due to the flat geometry of the prism sides, instead of an equilibrium contact line  
11 with constant contact angle (as in the case of cylinders at an interface), the triangular  
12 prisms leads to contact lines pinned at edges of the triangular face, as we discussed  
13 above. Bowing of thinner prisms leads to a contact line that is conformal to that of the  
14 bowed triangle surface. Thus a hexapole-like interface profile around them arises,  
15 wherein tips and edges of the triangle exhibit opposite interface height variations.  
16 Interestingly, the interface profile differs from that of ideal hexapoles, especially close to  
17 the prisms, due to the focusing of excess interface area near the tips. We find this to be  
18 the origin of the tip-to-tip attraction for same polarity prisms, which may be a useful  
19 mechanism to obtain regular open networks.

20 In contrast, we find thicker prisms to be much more flat, and thus the pinned  
21 contact line does not exhibit a significant hexapolar component. Instead, it likely  
22 generates an interaction, described by Fourier decomposition of the variability in  
23 interfacial height profile, as generated by non-ideal features of the flat surface, such as its  
24 roughness. This leads to quadrupole-quadrupole interactions at far field, consistent with  
25 our observation from the binding events.

### 26 *Open network structure and the path to capillary-drive self-assembly of ordered open* 27 *lattices*

28 The open networks shown in Fig. 14 display a heterogeneous structure,  
29 characterized by disordered strands and voids. These structures are reminiscent – and  
30 perhaps even more open than – networks self-assembled from colloidal ellipsoids at  
31 fluid-fluid interfaces<sup>10</sup>, which demonstrate enhanced rigidity as compared to close-  
32 packed arrays of isotropic spheres. Recent theoretical studies show unusual mechanical  
33 properties of regular open structures such negative Poisson's ratio in the twisted kagome  
34 lattice. Mechanical properties of these disordered open networks will be an interesting  
35 direction for future research.<sup>15,17,21,34,36</sup>

36 Open networks self-assembled from the three thinnest prisms, which exhibit  
37 polarity and possess a capillary hexapole, (Figs. 14a-c) are more heterogeneous than are  
38 networks self-assembled from the thickest prisms, which exhibit neither polarity nor a  
39 capillary hexapole (Fig. 14d). This is demonstrated quantitatively through the  
40 measurement of prism number density fluctuations (Fig. S5); open networks self-  
41 assembled from the thinnest prisms exhibit higher prism number density fluctuations than  
42 do open networks self-assembled from the thickest prisms. These results suggest that  
43 future work could understand how void structure in such disordered networks could be

1 controlled by design of building block shape, surface properties, and pair interactions in  
2 capillary systems.

3 On the other hand, to realize regular open networks, such as the kagome lattice,  
4 where only tip-tip binding is selected, further studies are needed in order to (1) select a  
5 single polarity component of the prisms, and (2) stabilize the binding of the prisms at the  
6 tip-tip configuration and avoid the collapse into edge-edge binding. The former may be  
7 addressed by introducing Janus character to the prisms, so that they attach to the interface  
8 in just one of the two possible configurations. The latter may be realized by optimizing  
9 the shape of the prisms such that the tips are slightly truncated such that the tip-tip  
10 configuration is a local minimum.

## 11 **Conclusion**

12 We have reported capillary-driven binding of thin, triangular prisms of T/L  
13 between 1/50 and 1/5 into open networks at a flat air-water interface. The interface pins  
14 to the concave face of the three thinnest prisms ( $T/L = 1/50$ ,  $1/25$ , and  $1/10$ ). Interface  
15 pinning and physical bowing of the thin prisms results in (a) two polarities corresponding  
16 to prism bowing up, interface pinned at top edges, prism center-of-mass below interface,  
17 and prisms bowing down, interface pinned at bottom edges, prism center-of-mass above  
18 interface, and (b) hexapolar-like interface profile around the prisms. The resulting  
19 capillary interactions between these triangular prisms lead to tip-tip, edge-edge, tip-edge,  
20 and edge-edge-offset pair binding events, depending on the polarity of the pair, and  
21 disordered open networks produced by self-assembly. Thick prisms ( $T/L = 1/5$ ) exhibit  
22 neither physical bowing nor splitting of the prisms into two subpopulations above and  
23 below the air-water interface. Prisms of all thicknesses self-assemble into open networks  
24 with void structure that depends on the geometric properties of the prism. The results can  
25 inform the design of thin prism building blocks for assembly of open networks at fluid-  
26 fluid interfaces with either order or disordered structure.

## 27 **Conflicts of Interest**

28 There are no conflicts of interest to declare.

## 29 **Acknowledgements**

30 This work was supported by the National Science Foundation under grant numbers NSF  
31 CBET 1232937 and NSF DMR 1609051. For eSEM imaging, we acknowledge the  
32 University of Michigan College of Engineering for financial support and the Michigan  
33 Center for Materials Characterization for use of the instruments and staff assistance.

34

1 **References**

- 2
- 3 1 N. Bowden, F. Arias, T. Deng and G. M. Whitesides, *Langmuir Langmuir*, 2001, **17**,
- 4 1757–1765.
- 5 2 N. Bowden, A. Terfort, J. Carbeck and G. M. Whitesides, *Science (80-. )*, 1997, **276**,
- 6 233–235.
- 7 3 P. Pieranski, *Phys. Rev. Lett. Phys. Rev. Lett. PRL*, 1980, **45**, 569–572.
- 8 4 G. Y. Onoda, *Phys. Rev. Lett. Phys. Rev. Lett. PRL*, 1985, **55**, 226–229.
- 9 5 J. Bae, N. P. Bende, A. A. Evans, J.-H. Na, C. D. Santangelo and R. C. Hayward, *Mater.*
- 10 *Horizons*, 2017, **4**, 228–235.
- 11 6 G. Soligno, M. Dijkstra and R. van Roij, *Phys. Rev. Lett.*, 2016, **116**, 258001.
- 12 7 G. Soligno, M. Dijkstra and R. van Roij, *Soft Matter*, 2018, **14**, 42–60.
- 13 8 T. S. Horozov, R. Aveyard, B. P. Binks and J. H. Clint, *Langmuir Langmuir*, 2005, **21**,
- 14 7405–7412.
- 15 9 T. S. Horozov, R. Aveyard, J. H. Clint and B. P. Binks, *Langmuir*, 2003, **19**, 2822–2829.
- 16 10 B. Madivala, J. Fransaer and J. Vermant, *Langmuir Langmuir*, 2009, **25**, 2718–2728.
- 17 11 J. C. Loudet, A. M. Alsayed, J. Zhang and A. G. Yodh, *Phys. Rev. Lett. Phys. Rev. Lett.*
- 18 *PRL*, 2005, **94**, 18301.
- 19 12 E. P. Lewandowski, J. A. Bernate, A. Tseng, P. C. Searson and K. J. Stebe, *Soft Matter*
- 20 *Soft Matter*, 2009, **5**, 886–890.
- 21 13 E. P. Lewandowski, M. Cavallaro, L. Botto, J. C. Bernate, V. Garbin and K. J. Stebe,
- 22 *Langmuir Langmuir*, 2010, **26**, 15142–15154.
- 23 14 B. Sun and Y. Yeo, *Curr Opin Solid State Mater Sci Curr. Opin. solid state Mater. Sci.*,
- 24 2012, **16**, 295–301.
- 25 15 G. N. Greaves, A. L. Greer, R. S. Lakes and T. Rouxel, *Nat. Mater.*, 2011, **10**, 823.
- 26 16 Y. Y. Wang, N. V Wheeler, F. Couny, P. J. Roberts and F. Benabid, *Opt. Lett.*, 2011, **36**,
- 27 669–671.
- 28 17 C. L. Kane and T. C. Lubensky, *Nat. Phys.*, 2013, **10**, 39.
- 29 18 S.-M. Kang, C.-H. Choi, J. Kim, S.-J. Yeom, D. Lee, B. J. Park and C.-S. Lee, *Soft Matter*
- 30 *Soft Matter*, 2016, **12**, 5847–5853.
- 31 19 M. P. and G. L. and N. Vandewalle, *New J. Phys.*, 2014, **16**, 23013.
- 32 20 Q. Chen, S. C. Bae and S. Granick, *Nature*, 2011, **469**, 381–384.
- 33 21 D. Z. Rocklin and X. Mao, *Soft Matter*, 2014, **10**, 7569–7576.
- 34 22 X. Mao, *Phys. Rev. E*, 2013, **87**, 62319.
- 35 23 J. Paulose, A. S. Meeussen and V. Vitelli, *Proc. Natl. Acad. Sci.*, 2015, **112**, 7639–7644.
- 36 24 B. Florijn, C. Coulais and H. van Martin, *Phys. Rev. Lett. Phys. Rev. Lett. PRL*, 2014,
- 37 **113**, 175503.
- 38 25 T. B<sup>o</sup>ckmann, M. Thiel, M. Kadic, R. Schittny and M. Wegener, *Nat Commun.* ,
- 39 DOI:Article.
- 40 26 J. A. Pelesko, *Self Assembly: The Science of Things That Put Themselves Together*,
- 41 Chapman and Hall/CRC, 2007.
- 42 27 G. M. Whitesides and B. Grzybowski, *Science (80-. )*, 2002, **295**, 2418–2421.
- 43 28 J. Dong, S. Chen, D. S. Corti, E. I. Franses, Y. Zhao, H. T. Ng and E. Hanson, *J. Colloid*
- 44 *Interface Sci.*, 2011, **362**, 33–41.
- 45 29 M. Mohammadi, E. D. Larson, J. Liu and R. G. Larson, *J. Chem. Phys.*, 2015, **142**.
- 46 30 M. E. Szakasits, W. Zhang and M. J. Solomon, *Phys. Rev. Lett.*, 2017, **119**, 58001.
- 47 31 J. Kim, X. Song, F. Ji, B. Luo, N. F. Ice, Q. Liu, Q. Zhang and Q. Chen, *Nano Lett.*, 2017,
- 48 **17**, 3270–3275.
- 49 32 A. Souslov, A. J. Liu and T. C. Lubensky, *Phys. Rev. Lett. Phys. Rev. Lett. PRL*, 2009,
- 50 **103**, 205503.
- 51 33 J. L. Atwood, *Nat Mater*, 2002, **1**, 91–92.

- 1 34 K. Sun, A. Souslov, X. Mao and T. C. Lubensky, *Proc. Natl. Acad. Sci.*, 2012, **109**,  
2 12369–12374.
- 3 35 D. Z. Rocklin, S. Zhou, K. Sun and X. Mao, *Nat. Commun.*, 2017, **8**, 14201.
- 4 36 T. C. L. and C. L. K. and X. M. and A. S. and K. Sun, *Reports Prog. Phys.*, 2015, **78**,  
5 73901.
- 6 37 M. Cavallaro, L. Botto, E. P. Lewandowski, M. Wang and K. J. Stebe, *Proc. Natl. Acad.*  
7 *Sci.*, 2011, **108**, 20923–20928.
- 8 38 V. N. Paunov, *Langmuir Langmuir*, 2003, **19**, 7970–7976.
- 9 39 K. A. Brakke, *Exp. Math. Exp. Math.*, 1992, **1**, 141–165.
- 10 40 J. C. Crocker and D. G. Grier, *J. Colloid Interface Sci.*, 1996, **179**, 298–310.
- 11 41 L. Botto, E. P. Lewandowski, M. Cavallaro and K. J. Stebe, *Soft Matter*, 2012, **8**, 9957–  
12 9971.
- 13 42 J. Ally, M. Kappl and H. J. Butt, *Langmuir*, 2012, **28**, 11042–11047.
- 14 43 N. Chatterjee and M. Flury, *Langmuir*, 2013, **29**, 7903–11.
- 15 44 C. W. Extrand and S. I. Moon, *Langmuir*, 2008, **24**, 9470–9473.
- 16 45 E. P. Lewandowski, P. C. Searson and K. J. Stebe, *J. Phys. Chem. B*, 2006, **110**, 4283–  
17 4290.
- 18 46 L. Yao, N. Sharifi-Mood, I. B. Liu and K. J. Stebe, *J. Colloid Interface Sci.*, 2015, **449**,  
19 436–442.
- 20 47 C. J. Dibble, M. Kogan and M. J. Solomon, *Phys. Rev. E Phys. Rev. E PRE*, 2006, **74**,  
21 41403.
- 22 48 P. Varadan and M. J. Solomon, *Langmuir*, 2003, **19**, 509–512.
- 23 49 M. H. Lee and E. M. Furst, *Phys. Rev. E*, 2008, **77**, 41408.
- 24 50 K. D. Danov, P. A. Kralchevsky, B. N. Naydenov and G. Brenn, *J. Colloid Interface Sci.*,  
25 2005, **287**, 121–134.
- 26 51 D. Stamou, C. Duschl and D. Johannsmann, *Phys. Rev. E*, 2000, **62**, 5263–5272.
- 27 52 T. Young, *Philos. Trans. R. Soc. London*, 1805, **95**, 65–87.
- 28 53 P.-G. de Gennes, F. Brochard-Wyart and D. Quéré, *Capillarity and Wetting Phenomena*,  
29 2004.
- 30 54 C. G. K., *Nature*, 1907, **75**, 361–362.
- 31 55 P. Singh and D. D. Joseph, *J. Fluid Mech.*, 2005, **530**, 31–80.
- 32 56 F. Dutka, M. Napiórkowski and S. Dietrich, in *Journal of Chemical Physics*, 2012, vol.  
33 136.
- 34  
35  
36  
37  
38  
39  
40  
41  
42  
43  
44  
45  
46  
47  
48  
49  
50

1 **Supplementary Information: Capillary-driven binding of thin triangular prisms at**  
 2 **fluid interfaces**

3 Joseph A. Ferrar, Deshpreet S. Bedi, Shangnan Zhou, Peijun Zhu, Xiaoming Mao,\* and Michael  
 4 J. Solomon\*

5 (Corresponding Author: [maox@umich.edu](mailto:maox@umich.edu) and [mjsolo@umich.edu](mailto:mjsolo@umich.edu))

6

7 **Multipolar interactions between particles at a fluid interface**

8 In this section we describe equilibrium interface shapes and the resulting capillary  
 9 interaction between circular multipoles. In the Results section we will show that the  
 10 capillary interaction between two triangular prisms in our experiment is similar to  
 11 hexapolar interactions.

12 The pressure difference across an interface between two stationary, immiscible fluids is  
 13 given by the Young-Laplace equation,

$$\Delta p = p_1 - p_2 = -\gamma \nabla \cdot \mathbf{n},$$

14 where  $\gamma$  is the surface tension and  $\mathbf{n}$  is the unit vector pointing from the lower fluid (2) to  
 15 the upper fluid (1). Note that  $-\nabla \cdot \mathbf{n} = 2H$ , where  $H$  is the mean curvature of the  
 16 interface surface. Suppose that the height of the interface is given by  $h(\mathbf{x})$ , where the far-  
 17 field equilibrium height of the interface is  $h = 0$  (the interface is flat and, consequently,  
 18 the pressure difference across the interface is zero). We can write the Young-Laplace  
 19 equation in terms of the height field as

$$\nabla \cdot \frac{\nabla h}{\sqrt{1 + |\nabla h|^2}} = \kappa^2 h$$

20 where

$$\kappa = \ell_c^{-1} \equiv \sqrt{\frac{(\rho_2 - \rho_1)g}{\gamma}}$$

21 is the inverse capillary length. The capillary length is a characteristic length scale arising  
 22 from comparing the relative strengths of gravitational acceleration and the surface  
 23 tension; for length scales much smaller than the capillary length, the effects of gravity  
 24 can be neglected. The capillary length of an air-water interface is 2.7 mm.

25 We can simplify the governing equation of the interface height  $h$  by making two  
 26 assumptions that are typically satisfied by micron-sized particles. First, the interface  
 27 slope is taken to be small:  $|\nabla h|^2 \ll 1$ . Second, we consider length scales that are much  
 28 smaller than the capillary length,  $l \ll \ell_c$ . In this case, the Bond number is vanishingly  
 29 small,  $\text{Bo} = (\kappa l)^2 \ll 1$ , and the Young-Laplace equation simplifies to the 2-D Laplace's  
 30 equation,

31 
$$\nabla^2 h = 0. \tag{1}$$

1 Let us consider the case of a solid particle adsorbed to the interface such that the  
 2 contact line between the interface and the particle surface is undulating. This can be due  
 3 to particle shape (anisotropies, corners, and edges) and surface roughness/irregularities.  
 4 These undulations can be decomposed into a multipole expansion such that this  
 5 differential equation can be solved analytically, for particles with circular cross-sections,  
 6 using polar coordinates  $(r, \theta)$ . The solution for the interface height profile is

$$7 \quad h(r, \theta) = H_0 \ln(\kappa r) + \sum_{m=1}^{\infty} H_m \left(\frac{r_0}{r}\right)^m \cos[m(\theta - \theta_{m,0})], \quad (2)$$

8 where  $H_m$  is the amplitude of the  $m$ th moment at the surface/circumference of the  
 9 particle's circular projection,  $r_0$ .  $m \in \mathbb{Z}^+ \cup \{0\}$  is the multipole moment, and  $m = 0, 1, 2, 3$   
 10 correspond to the monopole/charge, dipole, quadrupole, and hexapole moments,  
 11 respectively. If the particle adsorbed to the interface is sufficiently light, the monopole  
 12 moment vanishes; if the particle is allowed to spontaneously rotate about a horizontal  
 13 axis, then the dipole moment also vanishes. Therefore, the quadrupole moment ( $m = 2$ )  
 14 is typically the leading non-zero term in the multipole expansion (Figure ).

15 For two particles with circular cross-sections, it is convenient to use bipolar  
 16 coordinates  $(\omega, \tau)$  to obtain a solution to Eq.(1). They are defined implicitly via

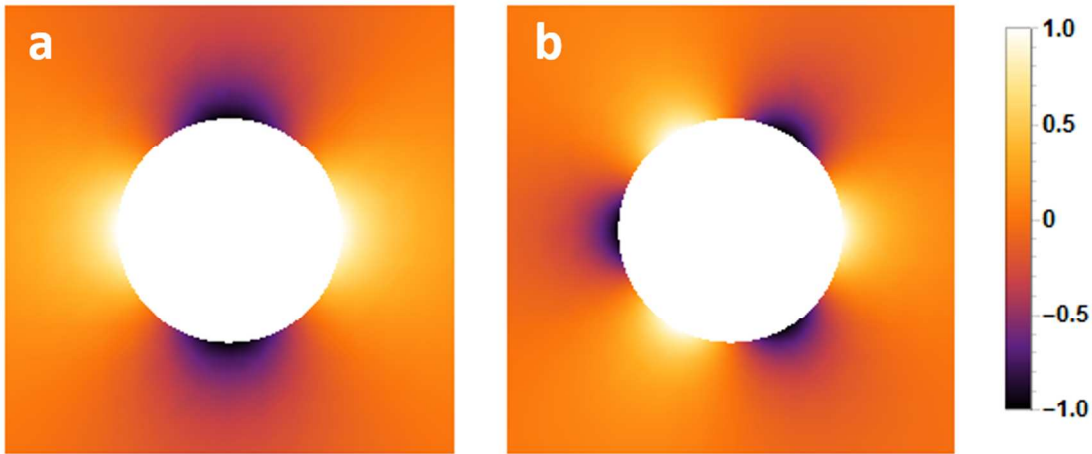


*Figure S1 . Theoretical interface height profile for particles with circular cross-sections. (a) A capillary quadrupole ( $m = 2$ ), with four alternating regions of positive and negative interface height (the equilibrium interface height far from any particles is taken to be zero), and (b) A capillary hexapole ( $m = 3$ ) with six alternating regions of positive and negative interface height.*

17  $x = a \frac{\sinh \tau}{\cosh \tau - \cos \omega}$ ,  $y = a \frac{\sin \omega}{\cosh \tau - \cos \omega}$ , where  $\tau \in \mathbb{R}$ ,  $\omega \in [0, 2\pi)$  (or, equivalently,  
 18  $\omega \in [-\pi, \pi)$ ). Curves of constant  $\omega$  and  $\tau$  are circles that intersect at right angles in the  
 19  $xy$ -plane.

20 The parameter  $a$  is determined by the particle radii and their separation distance

$$a^2 = \frac{1}{4r^2} [r^2 - (R_1 + R_2)^2] [r^2 - (R_1 - R_2)^2].$$

1 Note that, in the bipolar coordinate system, the circular projections of the contact lines on  
 2 the  $xy$ -plane are curves of constant  $\tau$ ,  $\tau = -\tau_1$  and  $\tau = \tau_2$ , where

$$\tau_1 = \cosh^{-1}\left(\frac{r^2 + R_1^2 - R_2^2}{2rR_1}\right), \quad \tau_2 = \cosh^{-1}\left(\frac{r^2 + R_2^2 - R_1^2}{2rR_2}\right)$$

3 Rewriting Laplace's equation in terms of bipolar coordinates ultimately yields a  
 4 deceptively simple partial differential equation of the form

$$\frac{\partial^2 h}{\partial \omega^2} + \frac{\partial^2 h}{\partial \tau^2} = 0.$$

5 The derivation can be found in Ref. 1<sup>1</sup> the resultant interface solution is

$$\begin{aligned} h(\omega, \tau) &= H_1 \sum_{n=1}^{\infty} A(n, m_1, \tau_1) \cos(n\omega - m_1\theta_1) \frac{\sinh[n(\tau_2 - \tau)]}{\sinh[n(\tau_1 - \tau_2)]} \\ &+ H_2 \sum_{n=1}^{\infty} A(n, m_2, \tau_2) \cos(n\omega - m_2\theta_2) \frac{\sinh[n(\tau_1 + \tau)]}{\sinh[n(\tau_1 + \tau_2)]} \end{aligned}$$

6 where

$$A(n, m_i, \tau_i) = m_i \sum_{k=0}^{\min(m_i, n)} \frac{(-1)^{m_i-k} (m_i + n - k - 1)!}{(m_i - 1)! (n - k)! k!} \exp[-(m_i + n - 2k)\tau_i].$$

### 7 *Interaction potential between two capillary multipoles*

8 The capillary interaction potential between two particles is a function of their orientations  
 9 and separation distance. It is given by

$$10 \quad U_{12} = \gamma(\delta S_{12} - \delta S_1 - \delta S_2), \quad (3)$$

11 where  $\delta S_{12}$  is the excess area created at the interface in the full two-particle system, and  
 12  $\delta S_i$  ( $i = 1, 2$ ) is the excess area in an isolated one-particle system (i.e., the separation  
 13 distance  $r \rightarrow \infty$ ). The excess area is defined as the difference between the actual surface  
 14 area  $\Sigma^*$  and the projected surface area  $\Sigma$  (the interface would be planar without the  
 15 deformation caused by the particle)<sup>2</sup> In the small slope regime, the excess surface area is  
 16 given by

$$\delta S = \frac{1}{2} \iint_{\Sigma} dS |\nabla h|^2.$$

17 From these two preceding equations, it is apparent that minimization of the  
 18 capillary interaction potential coincides with the minimization of excess area beyond that  
 19 created by two isolated particles. This favors the adoption of particle configurations such  
 20 that the slope of the resultant interface is reduced. For particles with fixed orientations,  
 21 the interaction between the two will be attractive if moving the particles closer together  
 22 will reduce the overall slope of the interface (and, thus, decrease the amount of excess

1 interfacial area) and repulsive if moving the particles further apart will reduce the overall  
 2 slope.

3 For a single particle with a circular cross-section and a contact line that is  
 4 undulating with multipole moment  $m$ , the excess surface area is <sup>1</sup>

$$\delta S_i = \frac{\pi}{2} m_i H_i^2.$$

5 For two capillary multipoles, the excess surface area is

$$\delta S_{12} = \pi [H_1^2 S_1 + H_2^2 S_2 - H_1 H_2 G \cos(m_2 \theta_2 - m_1 \theta_1)]$$

6 where

$$S_i = \sum_{n=1}^{\infty} \frac{n}{2} \coth[n(\tau_1 + \tau_2)] A^2(n, m_i, \tau_i)$$

$$G = \sum_{n=1}^{\infty} \frac{n A(n, m_1, \tau_1) A(n, m_2, \tau_2)}{\sinh[n(\tau_1 + \tau_2)]}$$

7 and

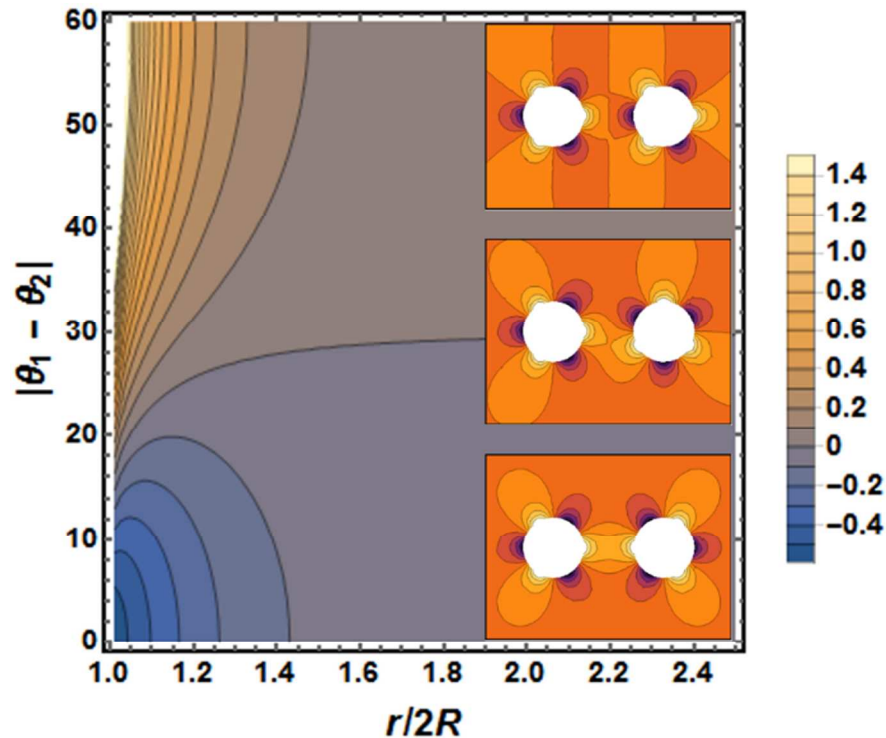


Figure S2 Theoretical capillary interaction potential between two capillary hexapoles as a function of separation distance,  $r$ , scaled by the diameter of the particles' circular projection,  $2R$ , and the particles' relative orientation,  $|\theta_1 - \theta_2|$ . The three insets show the interface height profile of three configurations corresponding to relative orientations of  $0^\circ$ ,  $30^\circ$ , and  $60^\circ$  at a distance of  $r/2R = 1.8$ .

$$A(n, m_i, \tau_i) = m_i \sum_{k=0}^{\min(m_i, n)} \frac{(-1)^{m_i-k} (m_i + n - k - 1)!}{(m_i - 1)! (n - k)! k!} \exp[-(m_i + n - 2k)\tau_i].$$

1 Here, it is important to realize that, for two capillary multipoles of the same order, such  
 2 that  $m_1 = m_2$ , the interaction energy reduces to a two-dimensional function of their  
 3 separation distance,  $r$ , and their *relative* orientation,  $|\theta_1 - \theta_2|$ . An example of hexapole-  
 4 hexapole interaction energy is shown in Figure S2.

#### 5 *Contact-line boundary conditions*

6 The solution to the Young-Laplace equation is subject to two boundary conditions: one at  
 7 the three-phase (solid, liquid, and fluid, with the latter oftentimes a gas) contact line and  
 8 one at the far boundary of the interface, infinitely far away. The latter is typically taken to  
 9 be the condition of a flat interface. The boundary condition at the contact line, however,  
 10 can be more complicated. In the simplest case, in which the surface of the solid phase  
 11 (e.g., a wall or a particle) is energetically homogeneous, the contact line is determined  
 12 such that the *equilibrium* contact angle,  $\theta_c$ , between the solid surface and the surface of  
 13 the interface is constant and satisfies the Young equation<sup>3,4</sup>

$$14 \quad \gamma \cos \theta_c = \gamma_{SG} - \gamma_{SL},$$

15 where  $\gamma, \gamma_{SG}, \gamma_{SL}$  are the liquid-gas, solid-gas, and solid-liquid surface tensions,  
 16 respectively.

17 In this paper, due to the specific shape of the particles used in the experiment – triangular  
 18 prisms – we will focus on a specific boundary condition in which the contact line is  
 19 kinetically trapped, or pinned, at sharp corners and edges of a particle. This pinning  
 20 results in a non-equilibrium contact angle that can deviate significantly from the  
 21 equilibrium contact angle discussed above and can also vary along the contact line. As  
 22 shown by Gibbs in an extension to the Young equation,<sup>5,6</sup> the non-equilibrium contact  
 23 angle,  $\theta_g$ , at a pinned edge can be any value in the range

$$24 \quad \theta_c \leq \theta_g \leq \pi - \delta + \theta_c,$$

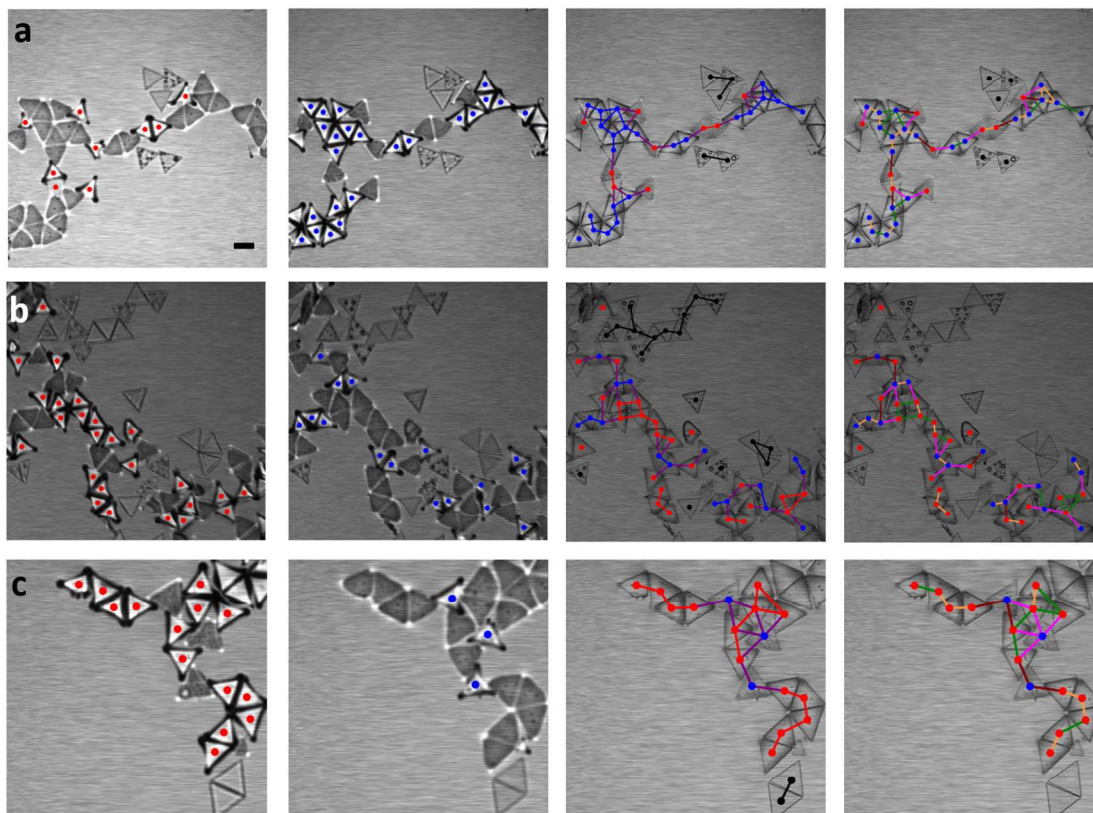
25 where  $\delta$  is the wedge angle of the particle. For instance, the wedge angle of the top or  
 26 bottom edges of a cube is  $\pi/2$ . Note that the limiting angles of Gibbs' criterion or  
 27 inequality are simply the equilibrium contact angles for each of the two surfaces that join  
 28 together to form the edge with a wedge angle of  $\delta$ ; when  $\theta_g$  extends beyond the bounds  
 29 of the inequality, the contact line becomes unpinned and begins to slide along one of the  
 30 two surfaces, as dictated by which bound was violated.<sup>7</sup> This phenomenon of contact-  
 31 line pinning has been observed in various experimental systems consisting of solid  
 32 particles or substrates containing sharp edges.<sup>8-10</sup> For example, in the case of a small  
 33 cylindrical particle with negligible Bond number oriented vertically, a preferred  
 34 equilibrium contact angle of  $\theta_c \neq \pi/2$  cannot be achieved anywhere along the side of the  
 35 cylinder; therefore, the contact line will either move up (if the preferred contact angle  
 36  $\theta_c < \pi/2$ ) or down (if  $\theta_c > \pi/2$ ) until either the top or bottom face, respectively, of the  
 37 cylinder coincides with the interface.<sup>11</sup> In this case, the contact line is pinned to the edge  
 38 of the cylinder with non-equilibrium contact angle  $\theta_g = \pi/2$ , and the surrounding  
 39 interface is completely planar.

1 In this experiment, the equilibrium contact angle of the air-water interface with the  
2 triangular prisms has been measured to be about 5 degrees, and the prisms have a wedge  
3 angle of 90 degrees (at both the top and the bottom). For these specific values, Gibbs'  
4 criterion ostensibly implies that mechanical equilibrium for a particle of negligible  
5 weight can only be satisfied when the contact line is pinned to the edges of the top face of  
6 a particle (as it is only here that the range of permissible contact angles allows for both  
7 upward- and downward-pointing interface/surface tension vectors such that they sum to  
8 zero over the closed contact line loop, as is required by the condition of mechanical  
9 equilibrium). Incorporating the fact that the triangular prisms are bowed, however, it can  
10 be seen that only downward-pointing interface vectors are possible if the contact line is  
11 pinned to the edges of the top face of a bowed-down prism – such a prism is only  
12 mechanically stable when the contact line is pinned to the edges of the *bottom* face  
13 instead. It remains true for a bowed-up prism, nevertheless, that the contact line  
14 necessarily is pinned to the edges of the top face. In both cases, then, the contact line  
15 needs to pin to the edges of the *concave* face of the bowed triangular prism, which is  
16 consistent with experimental observation.

### 17 **Triangular Prism Binding States Correlate with Prism Polarity**

18 In Tables 1 (as derived from Figure 6) and 2 (as derived from SI Figure S3), 237  
19 bonds are analyzed across six 1270 x 1270  $\mu\text{m}$  regions of open networks of  $T/L = 1/25$   
20 and  $1/50$  prisms (three 1270 x 1270  $\mu\text{m}$  regions per network). 17 bonds are between  
21 prisms with indeterminate polarity – prisms whose polarity cannot be resolved by optical  
22 microscopy – and are not included in this analysis. Of the 220 remaining bonds, there is  
23 perfect agreement in the number of bonds between prisms with the same polarity (133  
24 bonds) and prisms bound tip-tip or edge-edge (133 bonds), and there is also perfect  
25 agreement in the number of bonds between prisms with the opposite polarity (87 bonds)  
26 and prisms bound tip-edge or edge-edge offset (87 bonds).

27 Averaging over three locations in each network, and counting over the 237 total  
28 events, bonds between prisms with the same polarity account for 48% of all bonds for  
29  $T/L = 1/50$  prisms and 64% of all bonds for  $T/L = 1/25$  prisms; bonds between prisms  
30 with the opposite polarity account for 37% of all bonds for  $T/L = 1/50$  prisms and 36% of  
31 all bonds for  $T/L = 1/25$  prisms, and bonds between prisms with indeterminate polarity  
32 account for 15% of all bonds for  $T/L = 1/50$  prisms. Bonds of indeterminate polarity are  
33 not observed for  $T/L = 1/25$  prisms.



1

2 *Figure S3 Identification of triangular prism binding states for ( $T/L = 1/50$ ). Each row of*  
 3 *images (a) – (c) represents a different location within a network structure. The relative*  
 4 *position of microscope’s focal plane to the air-water interface is varied by column as*  
 5 *follows: Column (1): Microscope focal plane is  $\sim 200 \mu\text{m}$  below the interface. Clearly*  
 6 *visible prisms are identified with red markers. Column (2): Microscope focal plane is*  
 7  *$\sim 200 \mu\text{m}$  above the interface. Clearly visible prisms are identified with blue markers.*  
 8 *Column (3): Microscope focal plane is at the interface. Bonds between prisms with the*  
 9 *same polarity are identified with blue and red connecting lines, bonds between prisms*  
 10 *with the opposite polarity are identified with purple connecting lines, bonds between*  
 11 *prisms with indeterminate polarity are identified with black connecting lines. Column*  
 12 *(4): Microscope focal plane is at the interface. Prism-prism bonds are identified by their*  
 13 *polarity-independent orientation: side-side (orange connecting lines), tip-tip (green*  
 14 *connecting lines), side-side offset (brown connecting lines), tip-side (pink connecting*  
 15 *lines). Bonds in Columns (3) and (4) are tabulated in Table (2). Scale-bar is  $100 \mu\text{m}$ .*

16

17

Fig. No.	Relative polarity of bound prisms	No. of Bonds	% of each type of bond	tip-tip	edge-edge	No. of tip-tip + edge-edge	Correlation between relative polarity of bound prisms and bond orientation	tip-edge	edge-edge offset	No. of tip-edge + edge-edge offset	Correlation between relative polarity of bound prisms and bond orientation
5a	Same	10	50%	8	2	10	100%	0	0	0	0%
	Opposite	10	50%	0	0	0	0%	5	5	10	100%
	Indeterminate	0	0%	-	-	-	-	-	-	-	-
	Total	20									
5b	Same	32	66%	19	13	32	100%	0	0	0	0%
	Opposite	16	34%	0	0	0	0%	10	6	16	100%
	Indeterminate	0	0%	-	-	-	-	-	-	-	-
	Total	48									
5c	Same	36	67%	24	12	36	100%	0	0	0	0%
	Opposite	18	33%	0	0	0	0%	15	3	18	100%
	Indeterminate	0	0%	-	-	-	-	-	-	-	-
	Total	54									
Fig. 5	Same	78	64%	51	27	78	100%	0	0	0	0%
	Opposite	44	36%	0	0	0	0%	30	14	44	100%
	Indeterminate	0	0%								
	Total	122									

1

2 **Table S1.** Comparison of prism-prism bond type based on polarity of bound prisms and  
3 polarity-independent prism orientation for  $T/L = 1/25$ . All data is tabulated from  
4 analysis described in Fig. 5. Bonds are sorted into rows by the relative polarity of the  
5 bound prisms (same, opposite, or indeterminate polarity and into columns by the  
6 polarity-independent orientation of the bound prisms. The correlation between the  
7 relative polarity of the bound prisms and the polarity-independent bond orientation is  
8 calculated for network location analyzed. All bond types and correlations are also  
9 totaled over all 3 network locations.

10

Fig. No.	Relative polarity of bound prisms	No. of Bonds	% of each type of bond	tip-tip	edge-edge	No. of tip-tip + edge-edge	Correlation between relative polarity of bound prisms and bond orientation	tip-edge	edge-edge offset	No. of tip-edge + edge-edge offset	Correlation between relative polarity of bound prisms and bond orientation
6a	Same	23	58%	10	13	23	100%	0	0	0	0%
	Opposite	14	35%	0	0	0	0%	8	6	14	100%
	Indeterminate	3	8%	-	-	-	-	-	-	-	-
	Total	40									
6b	Same	20	41%	9	11	20	100%	0	0	0	0%
	Opposite	20	41%	0	0	0	0%	14	6	20	100%
	Indeterminate	13	27%	-	-	-	-	-	-	-	-
	Total	53									
6c	Same	12	48%	6	6	12	100%	0	0	0	0%
	Opposite	9	48%	0	0	0	0%	5	4	9	100%
	Indeterminate	1	5%	-	-	-	-	-	-	-	-
	Total	22									
Fig. 6 total	Same	55	48%	25	30	55	100%	0	0	0	0%
	Opposite	43	37%	0	0	0	0%	27	16	43	100%
	Indeterminate	17	15%								
	Total	115									

1

2 **Table S2.** Comparison of prism-prism bond type based on polarity of bound prisms and  
3 polarity-independent prism orientation for  $T/L = 1/50$ . All data is tabulated from  
4 analysis described in Fig. 6. Bonds are sorted into rows by the relative polarity of the  
5 bound prisms (same, opposite, or indeterminate polarity and into columns by the  
6 polarity-independent orientation of the bound prisms. The correlation between the  
7 relative polarity of the bound prisms and the polarity-independent bond orientation is  
8 calculated for network location analyzed. All bond types and correlations are also  
9 totaled over all 3 network locations.

10

## 11 Pair Binding Trajectories

12 Movies S1-S7 show pairwise binding trajectories analyzed in main text Fig. 10  
13 and 11, and in supplementary Fig. S4.

14 Movie S1:  $T/L = 1/50$  tip-tip, frame rate = 30 fps (Fig. S4a)

15 Movie S2:  $T/L = 1/50$  tip-edge, frame rate = 30 fps (Fig. S4b)

16 Movie S3:  $T/L = 1/25$  tip-tip trial 1, frame rate = 15 fps

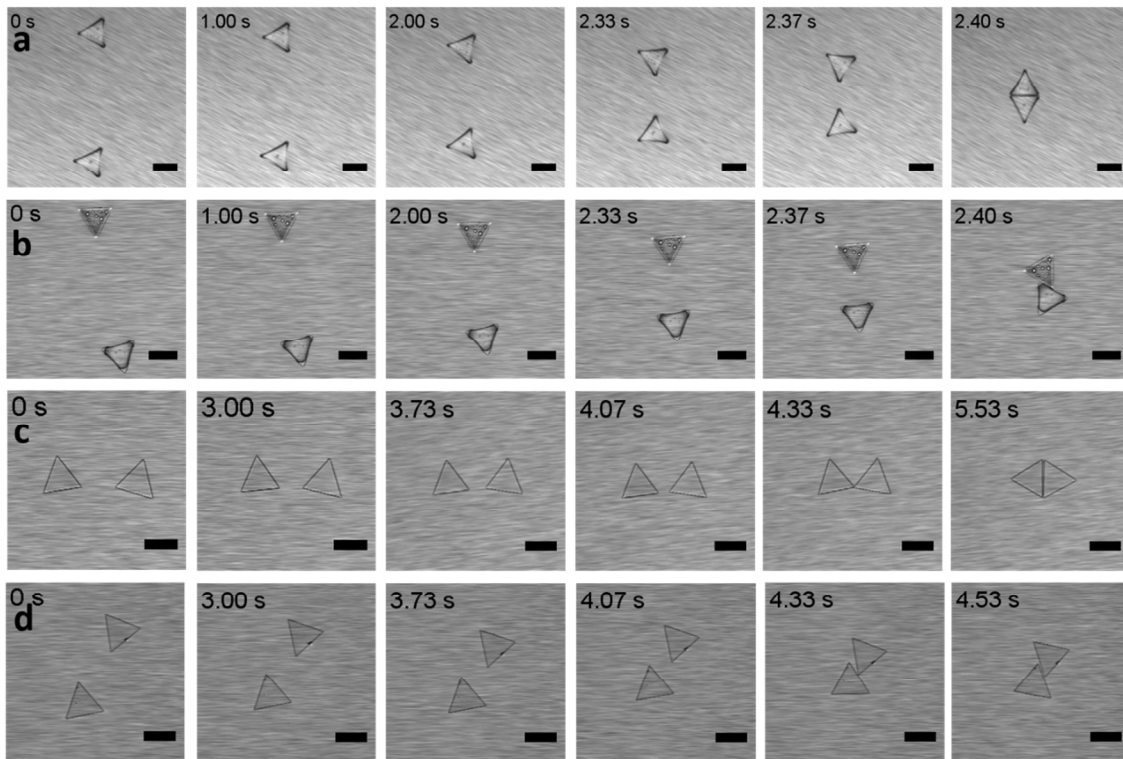
17 Movie S4:  $T/L = 1/25$  tip-tip trial 2, frame rate = 15 fps (Fig. S4c)

18 Movie S5:  $T/L = 1/25$  tip-tip trial 3, frame rate = 15 fps

19 Movie S6:  $T/L = 1/25$  tip-edge trial 1, frame rate = 15 fps

20 Movie S7:  $T/L = 1/25$  tip-edge trial 2, frame rate = 15 fps (Fig. S4d)

1



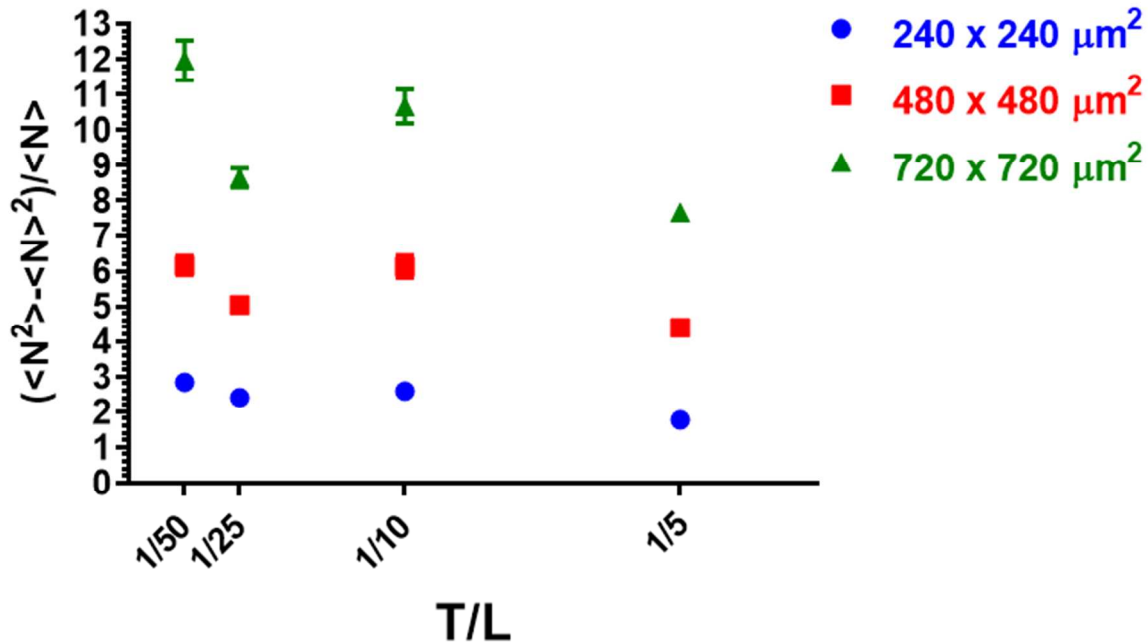
2

3 *Figure S4 Optical microscopy images of the 2 types of binding trajectories observed for*  
 4 *polar prisms ( $T/L \leq 1/10$ ), shown for  $T/L = 1/50$  (rows (a) and (b)) and  $T/L = 1/25$  (rows*  
 5 *(c) and (d)). For prisms of  $T/L = 1/50$  (rows (a) and (b)), contact occurs between the 5<sup>th</sup>*  
 6 *and 6<sup>th</sup> images of each row. For prisms of  $T/L = 1/25$  (rows (c) and (d)), contact occurs*  
 7 *in the 5<sup>th</sup> image of each row. Rows (a) and (c), tip-to-tip binding trajectory: the prisms*  
 8 *approach and first contact occurs at the tips. The prisms then rotate into a collapsed,*  
 9 *fully flush edge-to-edge orientation. Rows (b) and (d), tip-to-midpoint edge binding*  
 10 *trajectory: the prisms approach and contact one another in an orientation such that the*  
 11 *tip of one prism binds at the midpoint of the other prism's edge. The prisms then rotate*  
 12 *into an edge-to-edge orientation in which the two edges are offset from each other by  $L/2$ .*  
 13 *Scale bars are  $100 \mu\text{m}$ .*

14

## 15 Heterogeneity of Self-Assembled Networks

16 For regions of  $240 \times 240 \mu\text{m}^2$ , networks of the three thinnest prisms have a  
 17 compressibility measure of  $2.6 \pm 0.5$ , while the network of the thickest prisms has a  
 18 number density fluctuation of  $1.8 \pm 0.1$ . For regions of  $480 \times 480 \mu\text{m}^2$ , networks of the  
 19 three thinnest prisms have a number density fluctuation of  $5.8 \pm 0.6$ , while the network of  
 20 the thickest prisms has a number density fluctuation of  $4.4 \pm 0.2$ . For regions  $720 \times 720$   
 21  $\mu\text{m}^2$ , networks of the three thinnest prisms have a number density fluctuation of  $10.4 \pm$   
 22  $0.9$ , while the network of the thickest prisms has a number density fluctuation of  $7.7 \pm$   
 23  $0.2$ .



1

2 *Figure S5. Mean-squared prism number density fluctuation for the networks shown in*  
 3 *Figure 14.*

#### 4 Additional simulated pair-binding trajectories

5 Three representative initial conditions, corresponding to configurations close to (but  
 6 purposefully not exactly) tip-to-tip, tip-to-side, and side-to-side were selected, and the  
 7 resultant simulated trajectories are shown in Figure 15 for two different viscous-damping  
 8 coefficient ratios,  $\eta_{\bar{\theta}}/\eta_r = 1.46, 0.146$ . In all three sets of trajectories, it is clear that

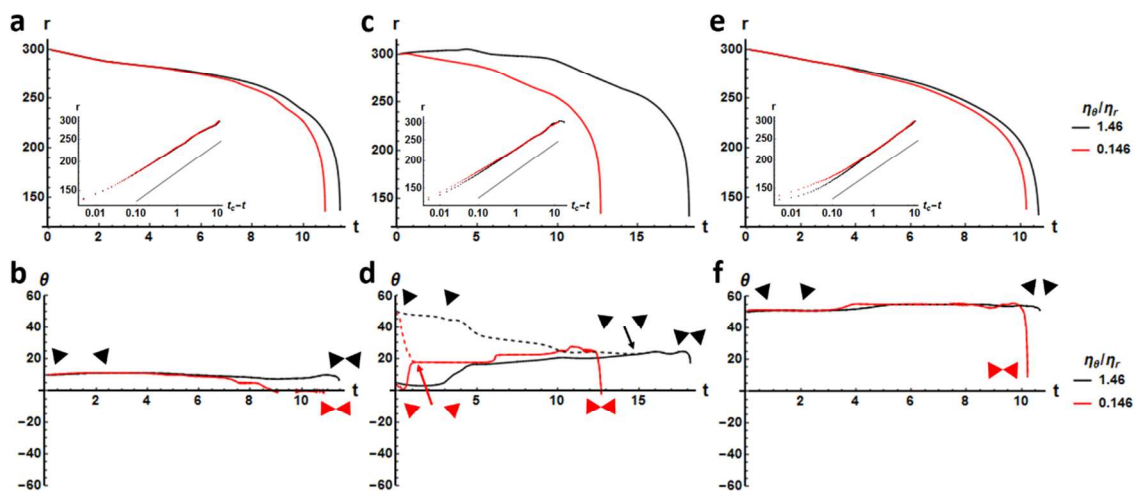


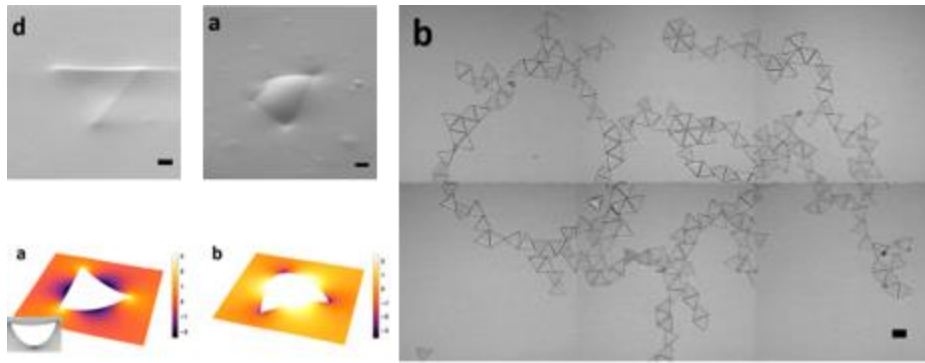
*Figure S6 Configuration trajectories for three representative initial conditions (close to (a),(b) tip-to-tip, (c),(d) tip-to-side, and (e),(f) side-to-side) and two different viscous-damping coefficient ratios. The top row shows the separation distance as a function of simulation time, with insets plotting separation distance values as a function of time-to-contact on a log scale. The gray reference line corresponds to the theoretical case of two ideal hexapoles approaching each other in a mirror-symmetric configuration. The bottom row shows the orientation angles of the triangular prisms as a function of simulation time.*

1 mirror symmetric configurations are preferred -- for cases where the initial configuration  
2 is already mirror symmetric, the subsequent configurations remain mirror symmetric;  
3 otherwise, the prisms will first rotate to a mirror symmetric configuration. For smaller  
4 ratios and fixed  $\eta_r$ ,  $\eta_{\bar{\theta}}$  becomes correspondingly smaller, meaning that it is easier for the  
5 prisms to rotate. This accounts for the fact that, in all cases, the  $\theta_1 = \theta_2 = 0^\circ$  tip-tip  
6 mirror-symmetric configuration is more easily achieved for the smaller ratio value.

## 9 References

- 10  
11 1 K. D. Danov, P. A. Kralchevsky, B. N. Naydenov and G. Brenn, *J. Colloid*  
12 *Interface Sci.*, 2005, **287**, 121–134.
- 13 2 D. Stamou, C. Duschl and D. Johannsmann, *Phys. Rev. E*, 2000, **62**, 5263–5272.
- 14 3 T. Young, *Philos. Trans. R. Soc. London*, 1805, **95**, 65–87.
- 15 4 P.-G. de Gennes, F. Brochard-Wyart and D. Quéré, *Capillarity and Wetting*  
16 *Phenomena*, 2004.
- 17 5 C. G. K., *Nature*, 1907, **75**, 361–362.
- 18 6 P. Singh and D. D. Joseph, *J. Fluid Mech.*, 2005, **530**, 31–80.
- 19 7 F. Dutka, M. Napiórkowski and S. Dietrich, in *Journal of Chemical Physics*, 2012,  
20 vol. 136.
- 21 8 J. Ally, M. Kappl and H. J. Butt, *Langmuir*, 2012, **28**, 11042–11047.
- 22 9 N. Chatterjee and M. Flury, *Langmuir*, 2013, **29**, 7903–11.
- 23 10 C. W. Extrand and S. I. Moon, *Langmuir*, 2008, **24**, 9470–9473.
- 24 11 E. P. Lewandowski, P. C. Searson and K. J. Stebe, *J. Phys. Chem. B*, 2006, **110**,  
25 4283–4290.

26



Thin, triangular prisms self-assemble into open networks via capillary interactions at flat air-water interfaces